Linear time periodic system approximation based on Floquet and Fourier transformations for operational modal analysis and damage detection of wind turbine

Ambroise Cadoret, Enora Denimal Goy, Jean-Marc Leroy, Jean-Lou Pfister, Laurent Mevel

Linear time periodic system approximation based on Floquet and Fourier transformations for operational modal analysis and damage detection of wind turbine

Ambroise Cadoret[a,b], Enora Denimal Goy[b], Jean-Marc Leroy[a], Jean-Lou Pfister[c], Laurent Mevel[b,*]

[a] *IFP Energies nouvelles, 69360 Solaize, France*
[b] *Université Gustave Eiffel, Inria, COSYS-SII, I4S, 35042 Rennes, France*
[c] *IFP Energies nouvelles, 92852 Rueil-Malmaison, France*

Abstract

Operational Modal Analysis (OMA) identifies modal properties of mechanical structures from vibration data collected from a few sensors under operation conditions. These methods are widely used to monitor civil engineering structures that are modeled as time-invariant systems. However, when dealing with wind turbines and rotating machines, many dedicated OMA techniques were developed to deal with the time-periodic behavior. Existing methods pre-process the data to adapt them to classical identification techniques. Yet, these methods present limitations as either requiring a high number of measured rotation periods, assuming the assumption of an isotropic rotor (i.e. undamaged), or the knowledge of the rotational speed. This work proposes to lift these difficulties by proving that the application of the classical system identification methods can produce meaningful estimates for anisotropy monitoring. This observation is based on directly approximating the time-periodic dynamic behavior of the wind turbine as a properly defined time-invariant system under periodic inputs. It results in the possibility of using classical identification methods without modification to retrieve the system matrices of the approximated time-invariant system. This approach does not require knowing the rotor speed, requiring relatively fewer measurements and it is not restricted to isotropic rotors. The identified modes can be used reliably for the monitoring of operating wind turbines and more especially for fault detection, at the expense of losing a part of the complete description of the periodic system. The resulting anisotropy monitoring approach and its capacities are illustrated in two cases. Firstly, on an academic model of a wind turbine and then on an aero-servo-elastic numerical model of a rotating 10MW wind turbine to demonstrate the ability of the method to deal with realistic and representative data. It is shown for the latest case, from sensors located on the blades of the wind turbine, the approach is able to identify correctly the system properties (frequencies and mode shapes) and is also able to detect efficiently a fault on a blade.

Keywords: Operational Modal Analysis, Wind Turbine, Subspace Methods, Fault detection, Floquet decomposition

1. Introduction

Considering the forecasted increase in the number of wind farms in the coming years, it is important to implement reliable fault detection methods based on data collected during operation. The methods based on

*Corresponding author; *E-mail address: laurent.mevel@inria.fr*

Operational Modal Analysis (OMA) for Linear Time-Invariant (LTI) structures are part of the solution. There are already many OMA methods developed for civil engineering, for LTI systems, in frequency or time domain [8]. The transposition of those methods to those new rotating systems is not straightforward. Indeed, the rotor rotation of a wind turbine breaks the LTI hypothesis, and these systems should rather be modelled as linear time periodic (LTP) systems. As they no longer meet the basic OMA assumptions, the extension of these LTI-based OMA methods to LTP systems should be considered.

In this context, the first method developed for OMA of wind turbines is the Multi-Blade Coordinate (MBC) method [6]. It is based on a change of variables to transform an LTP system into an LTI system, making classical OMA methods applicable. However, using the MBC transform to obtain the Floquet modes is valid only if the rotor is isotropic, i.e. when all the blades have the same properties and the external conditions are isotropic, which is not verified by experiment [34]. The MBC transform will always transform the state and output from the rotating to the ground-fixed frame, but the system matrices will become time-invariant only in the isotropic case. Indeed, the MBC modes and Floquet modes are not equal for every rotor configuration and every anisotropy state [29], which makes the MBC modes non-adapted to monitor the structure based on the Floquet modes or any derived feature. Another method for wind turbines is based on the so-called harmonic transfer function (HTF) [2]. The approach was originally defined for control purposes [39], to create a map between the inputs and outputs of an LTP system. It pre-processes the measurements to increase the dimension of the outputs by defining the Exponentially Modulated Periodic (EMP) signal space. The theoretical number of modulation is a priori unknown and must be tuned by the user. Moreover, this number increases with higher levels of anisotropy. Also, the main problem of the HTF is the assumption of well-separated modes, which is stressed when the spectrum is shifted by integers multiple of the rotor speed. This method has been extended to subspace identification with the same pre-processing [35]. The drawback of this method is that it requires an increase of the dimension of the observation space, as a consequence of the required formalism, leading to a high computational cost. This method requires knowledge of the actual rotational speed of the system, which is assumed to be unmeasured in the present paper. Finally, the last type of OMA method for wind turbines is based on classical subspace methods adapted to LTP systems, namely the SSI-LPTV method [16], the partial Floquet Analysis [28], or the PO-MOESP method [26]. These methods identify the modes of an LTP system and do not require a pre-processing of the measurements, such as collecting the data according to the period, or isotropic properties of the rotor. However, knowing the rotational speed, the identified modes converge to their theoretical value with a rate depending on the number of rotational periods. Consequently, these methods are adapted for systems with high rotational speed, such as helicopters, but poorly suitable for systems with low rotational speed such as wind turbines. All these mentioned above methods are modifications of classical frequency or time domain identification methods without solving all problems and sometimes introducing constraints and artefacts [40]. Finally, notice that classical identification methods for LTI systems have been used on data from the rotor without any pre-processing [21], despite a priori not satisfying all the required assumptions. The existence of such works has led this current paper to investigate if and why classical system identification methods developed for LTI systems can produce meaningful results for the monitoring of wind turbines and clarify the obtained results. In this context, the objective of the paper is to present an appropriate modeling of LTP systems that enables the identification and monitoring of such systems with reliable indicators through the classical identification methods.

The first theoretical contribution is dedicated to the demonstration that such modeling exists. Then, the second theoretical contribution is to demonstrate how it can be exploited for the identification and monitoring of a wind turbine. Section 2 and 3 are then devoted to show the relation between a model-based truncated Fourier-Floquet modeling and the LTI modes identified through the unmodified SSI approach developed for LTI systems [23].

The approximation proposed here is based on the use of the Floquet theory coupled with a Fourier decomposition to transform the LTP system into an LTI system. Indeed, according to the Floquet theory [12], the dynamical response of an LTP system can be defined as a sum of terms of periodic amplitudes, the so-called Floquet modes. Because of this periodicity, these modes can be expanded into Fourier series with an infinity of components. A system composed of an infinity of Fourier components with constant amplitude (identical to the modes of an LTI system) would theoretically be equivalent to an LTI system of infinite dimension. However, [1] shows (with an application on the Mathieu oscillator) that only some Fourier components are needed to characterize a Floquet mode. Thus, by selecting for each Floquet mode only the Fourier components with high contribution, the LTP system can be approximated by an LTI system of finite dimension. To obtain this result, in Section 2 the approximation of the free vibrations corresponding to the LTP systems is defined in order to give a physical meaning to the LTI modes that are corresponding to this approximation. It then relates the Floquet modes of an LTP system to their truncated Fourier decomposition. Notwithstanding, in Section 2, the defined approximation is only applied on the homogeneous part, i.e. the transition and observation matrices. Then, it is established that the complete LTP modeling can be approximated by an LTI model under periodic inputs. In Section 3, the input and feedthrough matrices remain periodic. Thus, it yields an LTI system subjected to nonstationary input, namely a periodic input, which still does not satisfy the assumptions of classical OMA methods defined for the full LTI systems. Nonetheless, thanks to the periodic nature of the inputs, Section 3 proves that the system matrices (A,C) of this model of an LTI system under inputs with periodic moments can still be identified by applying the classical SSI approach previously developed for full LTI systems [23] and its corresponding uncertainty estimation method [24].

It has to be noted that previous works already attempted to express an LTP system as an LTI system, and that the approximation proposed here is different from those works. Indeed, in the time domain, the time-lifted representation and the cyclic reformulation are expressing the system as a time-invariant based on the periodic behavior of the system matrices [7]. Both lead to an increase in the dimension depending on the discrete period of the system. They require to know the period of rotation, they also lead to observation data of higher dimension, which may lead to memory burden and loss of numerical precision for the system identification. Another possibility is to use the frequency lifted reformulation based on the Fourier series decomposition of the system matrices and the EMP signal [7, 27]. Theoretically, with this representation, the dimension of the new system matrices is infinite, as the Fourier series decomposition of the periodic matrices is also infinite.

Thanks to the approximation developed in Section 2 and the proof of the viability of applying the classical SSI approach together with the computation of the corresponding uncertainty estimation in Section 3, it is demonstrated that the identification of the truncated Fourier decomposition of the Floquet modes as LTI modes is possible, as well as using them to monitor a wind turbine in operation to track the appearance of structural faults. More precisely, a possible indicator for monitoring the health of a wind turbine rotor is its anisotropy (or imbalance) [32]. The rotor anisotropy can be the consequence of a pitch angle misalignment, an ice accumulation,

or a structural fault. These three causes lead to different behaviors of the structure and the first two have been largely studied [5, 18]. Considering structural faults, previous works have proposed to model it as a change in a blade stiffness to generate the anisotropy and studied the impact on the dynamical behaviour [19]. It has been shown that the anisotropy can be seen through two indicators, namely the apparition of new components in the Floquet modes in the fixed frame (nacelle and tower) and the change of amplitude and phase shift between blades in the LTI whirling modes [32]. Note that the change of phase shift is more than 10 times more sensitive than the change of frequency [9], making it an interesting feature for wind turbine monitoring. Consequently, the monitored features will be restricted and focused on the change of amplitude and phase shift in the following. Thus, the final contribution of this paper is to illustrate the reliability and interest of the Floquet-Fourier approximation for the anisotropy detection through the tracking of those two quantities using the blade roots moments of a multi-physics model of a wind turbine. The LTI mode shapes of the reference structure (considered healthy) are compared to the current (possibly damaged) identified LTI modes by studying phases and amplitudes change while computing the corresponding uncertainties computed thanks to a newly established sensitivity-based numerical scheme. Finally, the LTI modes are also compared with the Modal Assurance Criterion (MAC) and its associated uncertainty computation [14] to validate this anisotropy detection method and thus demonstrate its effectiveness for wind turbine monitoring.

The organisation of the paper is as follows. Section 2 presents the dynamical behavior of an LTP system, its approximation by an LTI system with a Floquet-Fourier transformation and the validation of the approximation with an example on a theoretical model of a wind turbine. Section 3 defines the state space representation of the approximation by an LTI system under inputs with periodic moments and the applicability of the Stochastic Subspace Identification (SSI) for the identification of the approximation is assessed. Then, Section 4 illustrates that classical OMA methods can be used to identify the LTI modes of the approximation, with examples on data computed with an aero-servo-elastic wind turbine model. Section 5 assesses the impact of the rotor anisotropy on the LTI modes. Finally, Section 6 defines a method for rotor anisotropy detection using blade root moments and their Gaussian confidence intervals. Then, the method is validated with the detection of a drop of 5% of the global stiffness of a blade and tested for the detection of 20% of local stiffness drop.

2. Linear Time Periodic (LTP) system approximation

2.1. Dynamic model

Let us consider a wind turbine whose rotor is supposed to rotate at a constant speed (rotation period T), and note $\xi(t) \in \mathbb{R}^m$ the displacement vector at the degrees of freedom (DOF) of the system describing the small vibrations of the structure about the periodic equilibrium induced by the balance between internal and external loads. The time evolution of these small fluctuations can be expressed as a linear time-periodic system

$$\mathcal{M}(t)\ddot{\xi}(t) + \mathcal{C}(t)\dot{\xi}(t) + \mathcal{K}(t)\xi(t) = v(t), \tag{1}$$

where $\mathcal{M}(t)$, $\mathcal{C}(t)$, and $\mathcal{K}(t)$ are respectively the T-periodic mass, damping and stiffness matrices. The unknown input $v(t)$ is assumed to be a Gaussian white noise, that models the small random fluctuations of the aerodynamic forces due to atmospheric turbulence. In the following, the mechanical system is expressed in a state space form,

from the definition of the state vector $x(t) \in \mathbb{R}^n$ where $n = 2m$ and the observation $y(t) \in \mathbb{R}^r$.

$$x(t) = \begin{bmatrix} \xi(t) \\ \dot{\xi}(t \end{bmatrix} \quad \text{and} \quad y(t) = C_a\ddot{\xi}(t) + C_v\dot{\xi}(t) + C_d\xi(t) + w(t), \tag{2}$$

where C_a, C_v and C_d are selection matrices. Note that because of the rotation, some components of y may correspond to measures of vibration in a non-inertial frame. A Gaussian white noise $w(t)$ modeling measurement noise has also been added to the observation equation. This leads to the following state space expression:

$$\begin{cases} \dot{x}(t) = A_c(t)x(t) + B_c(t)v(t) \\ y(t) = C(t)x(t) + D(t)v(t) + w(t) \end{cases}, \tag{3}$$

with

$$A_c(t) = \begin{bmatrix} 0 & I \\ -\mathcal{M}(t)^{-1}\mathcal{K}(t) & -\mathcal{M}(t)^{-1}\mathcal{C}(t) \end{bmatrix}, \quad C(t) = \begin{bmatrix} C_d - C_a\mathcal{M}(t)^{-1}\mathcal{K}(t) & C_v - C_a\mathcal{M}(t)^{-1}\mathcal{C}(t) \end{bmatrix},$$
$$B_c(t) = \begin{bmatrix} 0 \\ -\mathcal{M}(t)^{-1} \end{bmatrix} \quad \text{and} \quad D(t) = C_a\mathcal{M}^{-1}(t).$$

All matrices are periodic with period T, with $A_c(t) \in \mathbb{R}^{n\times n}$, $C(t) \in \mathbb{R}^{r\times n}$, $B_c(t) \in \mathbb{R}^{n\times m}$ and $D(t) \in \mathbb{R}^{r\times m}$.

2.2. Floquet theory of periodic systems

The general solution of the stochastic differential equation (3) can be expressed as the sum of the homogeneous solution and of the forced response [31]:

$$x(t) = \Phi(t, t_0)x(t_0) + \int_{t_0}^{t} \Phi(t, \tau)B_c(\tau)v(\tau)d\tau, \tag{4}$$

where $\Phi(t, t_0)$ is the so-called *fundamental matrix*, solution of the initial-value problem $\Phi(t_0, t_0) = \mathbf{I}$, $\partial_t\Phi = A_c(t)\Phi(t, t_0)$ for $t > t_0$.

Floquet theory [12] gives the necessary tools to deal with the present case where $A_c(t)$ is T-periodic. The authors refer the reader to [29, 30] for more details and only provide the main results here. Within Floquet's framework, the fundamental matrix evaluated at time $t_0 + T$ is defined as the *monodromy matrix*, noted $Q(t_0) = \Phi(t_0 + T, t_0)$, and plays a special role. According to the theory, there exists indeed a (non-unique) T-periodic matrix $t \mapsto P(t, t_0)$ such that

$$\Phi(t, t_0) = P(t, t_0) \exp\left(\frac{t}{T}\log(Q(t_0))\right). \tag{5}$$

A modal decomposition of the monodromy matrix $Q(t_0)$ allows therefore to expand this expression in terms of modes. Noting λ_i the eigenvalues of $Q(t_0)$ — that are independent of t_0 — and $\Psi(t_0)$ the matrix of eigenvectors (stacked in columns), and assuming that all eigenvalues are simple, $Q(t_0) = \Psi(t_0)[\lambda]\Psi(t_0)^{-1}$, where $[\lambda]$ is the diagonal matrix having the λ_i's as entries. Now introducing the *Floquet characteristic exponents* μ_i such that

$$\exp(\mu_i T) = \lambda_i, \tag{6}$$

defined up to a relative integer multiple of $\Omega = 2\pi/T$ and setting $t_0 = 0$, the fundamental matrix takes the following expression:

$$\Phi(t, 0) = P(t, 0)\Psi(0) \exp\left(t[\mu]\right) \Psi(0)^{-1}. \tag{7}$$

Let us eventually note $q_j(0) = \psi_j(0)x(0)$ — where $\psi_j(0)$ is the j–th row of the matrix $\Psi(0)^{-1}$ — and $X_j(t) = P(t,0)\psi_j(0)$ a T-periodic *mode shape*. Then, the homogeneous solution $x_h(t) = \Phi(t,0)x(0)$ can be expressed as:

$$x_h(t) = \sum_{j=1}^{n} X_j(t) \exp(\mu_j t)\, q_j(0). \tag{8}$$

The periodic mode shape can be further expanded in a Fourier series as

$$X_j(t) = \sum_{l=-\infty}^{\infty} X_{j,l} \exp(il\Omega t). \tag{9}$$

By combining Equations (8) and (9), the homogeneous can be expressed as

$$x_h(t) = \sum_{j=1}^{n} \sum_{l=-\infty}^{\infty} X_{j,l} \exp((\mu_j + il\Omega)t)\, q_j(0). \tag{10}$$

The homogeneous solution shown here implies that an LTP system has a finite number of modes, and each mode has an infinite number of harmonics, which are the Fourier components of the Floquet modes.

2.3. Approximation of the Floquet modes

Once the Floquet mode decomposition is done, the objective is to express the observation vector as a finite sum of terms to obtain the description of a time invariant system. The Floquet mode decomposition of the observation $y_h(t) = C(t)x_h(t)$ writes

$$y_h(t) = \sum_{j=1}^{n} Y_j(t) \exp(\mu_j t)\, q_j(0), \tag{11}$$

where $Y_j(t) = C(t)X_j(t)$ is the observed amplitude of the j–th Floquet mode and is a periodic vector of period $T = \frac{2\pi}{\Omega}$, which can then be expanded into a Fourier series:

$$Y_j(t) = \sum_{l=-\infty}^{\infty} Y_{j,l} \exp(il\Omega t) \tag{12}$$

By combining Equations (11) and (12), the observation vector can be expressed as an infinite sum of terms:

$$y_h(t) = \sum_{j=1}^{n} \sum_{l=-\infty}^{\infty} Y_{j,l} \exp((\mu_j + il\Omega)\, t)\, q_j(0) \tag{13}$$

Most relevant components of the expansion of $y_h(t)$ are determined by the participation factor [25], which is the normalized norm of the Fourier components of the periodic mode shape. This metric between 0 and 1 gives for all the Fourier components the weight of the Fourier components in the periodic mode shape and is defined as:

$$\phi^y_{j,l} = \frac{\|Y_{j,l}\|^2}{\sum_{k=-\infty}^{\infty} \|Y_{j,k}\|^2}. \tag{14}$$

By defining a minimal participation factor threshold (ϕ^y_{min}), an approximation of the observation ($\hat{y}_h(t)$) is constructed as a finite sum of terms,

$$\hat{y}_h(t) = \sum_{(j,l),\phi^y_{j,l} \geq \phi^y_{min}} Y_{j,l} \exp((\mu_j + il\Omega)\, t)\, q_j(0), \tag{15}$$

$\hat{y}_h(t)$ can then be expressed as

$$\hat{y}_h(t) = \sum_{p=1}^{\tilde{n}} Y_p \exp(\bar{\mu}_p t)\, q_p(0), \tag{16}$$

where each index p corresponds to a pair (j, l) and $\bar{\mu}_p = \mu_j + il\Omega$ and $\tilde{n}$ is the number of Fourier components with a participation factor greater than the minimum threshold ϕ^y_{min}.

Finally, the Floquet modes of an LTP system have been approximated by a finite number of terms identical to those of an LTI system. Consequently, the free response of an LTP system can be approximated by the behavior of an LTI system, as it was illustrated in [1] with the Mathieu oscillator. It should be noted that the participation factors, and in turn this approximation, are very dependent on the choice of the output channels [26].

2.4. Numerical validation of the approximated model

The previously defined approximation is tested and validated on a phenomenological model of a wind turbine. Firstly, a frequency domain study is performed to verify that the frequencies obtained with the approximation model fit the frequencies of the real model. Secondly, the error of the approximation looking at the periodic mode shapes is computed. Here, a model of wind turbine with five DOF is used [29], with the same structural parameters as described therein and a rotational speed of 1.4 rad/s. The model is composed of one DOF of flap bending for each blade and two DOF for the tilt and yaw motion of the nacelle. To compute the fundamental matrix ($\Phi(t, t_0)$) and then the monodormy matrix ($Q(t_0)$), the homogeneous part of Equation (3) is integrated ten times for linearly independent initial conditions $\Phi(0, t_0) = I$. For this example the approximation is computed with a minimum participation factor (ϕ^y_{min}) of 1% using the acceleration of all the DOF as outputs. A summary of the approximation is given in Table 1, where the sum of the participations of the Fourier components of each Floquet mode is above 0.999. Also, the Fourier components inside the interval [-1,1] that have a participation factor lower than ϕ^y_{min} are added. They are associated with the id number 13, 14, and 15.

Floquet mode	id Number	Harmonic number	Participation factor	Frequency (Hz)	Damping (%)
Yaw motion	1	1	0.598	1.693	0.690
	2	0	0.243	1.470	0.794
	3	-1	0.159	1.248	0.936
Pitch/tilt motion	4	1	0.409	1.813	0.598
	5	0	0.300	1.590	0.682
	6	-1	0.291	1.367	0.794
Forward flap	7	-1	0.632	0.641	0.324
	8	0	0.233	0.864	0.240
	9	1	0.134	1.087	0.191
Collective flap	10	0	1.000	0.746	0.267
	13	1	0	0.969	0.205
	14	-1	0	0.523	0.0.380
Backward flap	11	1	0.990	0.670	0.230
	12	0	0.010	0.448	0.344
	15	-1	0	0.225	0.685

Table 1: Fourier components of Floquet modes of the approximation, with a minimal participation factor of 1% and the Fourier components inside the interval [-1,1], for a rotational speed of 1.4 rad/s

The objective is to verify that the natural frequencies of the identified LTI modes ($\frac{|\bar{\mu}_p|}{2\pi}$) are comparable to those of the wind turbine model (computed from the model). The identified frequencies of the wind turbine are obtained based on a decay test (non-zero initial displacements and zero load). Precisely, these frequencies are obtained by analysing the frequency peaks in the Power Spectral Density (PSD) of the response. This comparison is illustrated for the 5DOF wind turbine in Figure 1, where the PSDs of the accelerations of one

rotor DOF and one tower DOF are represented. The frequencies obtained from the approximation given in Table 1 are represented with dashed lines and referred by their id number.

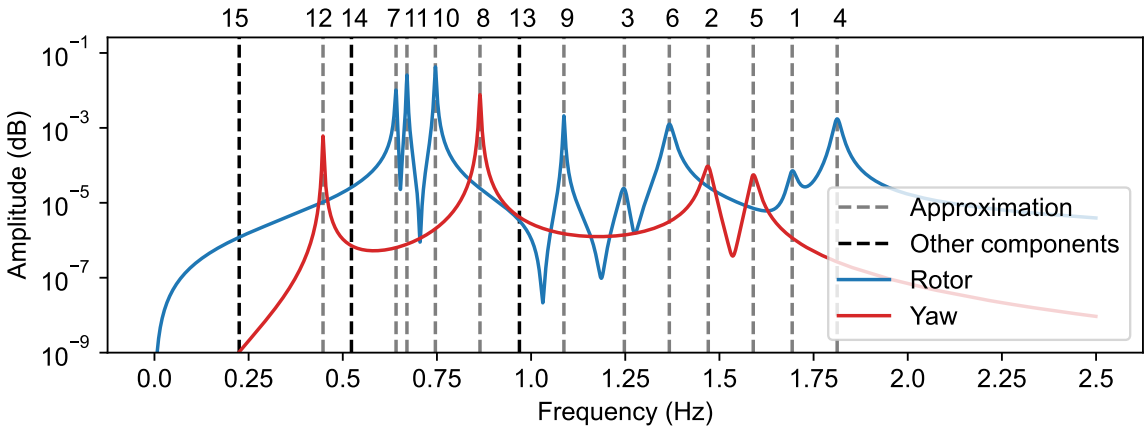

Figure 1: Comparison of the frequencies from Table 1 (dashed lines and id number) and the Power Spectral Density (PSD) of a free decay of the 5DOF wind turbine of a rotor DOF (blue line) and a tower DOF (red line) – (ϕ_{min}) threshold of 1%

As seen in Figure 1, each peak in the PSD spectrum corresponds to one of the frequencies from the model LTI modes (the model LTI modes are the Fourier components expressed in modal form, i.e. defined by a mode shape, a frequency, and a damping). And vice versa, all model LTI modes are observable in the PSD. Moreover, a good alignment between the frequency peaks and the approximation is observable. To conclude, as the Floquet modes can be described by a finite sum of LTI modes (i.e. the Fourier components with a non-negligible participation factor), approximating the homogeneous part of an LTP system as an LTI system is plausible.

A method to evaluate the approximation error is developed to compare the exact periodic mode shapes with those reconstructed with the approximation. The exact Floquet modes Y_j are compared to the inverse Fourier transform applied to the sum of the Fourier components retained in the approximation. For the approximation (Table 1), the relative approximation error ($\frac{\|Y_j(t)-\hat{Y}_j(t)\|}{\|Y_j(t)\|}$) over the period is below 0.05%, for all the DOF and for all the Floquet modes. So, in this example, the Floquet modes are well approximated.

In Figure 2, the first reconstructed periodic mode shape is compared to the exact one on two DOFs, one of the rotor and one of the tower. To illustrate the impact of the truncation on the approximation, different minimum participation factor thresholds ϕ^y_{min} are considered. It is clear that the lower the participation factor, the better the approximation. Indeed, when ϕ^y_{min} is lower, more Fourier coefficients are retained in the approximation and so a higher accuracy is reached. In the present case, a minimum participation factor of 0.1 is required to obtain an accurate approximation. This can be confirmed with an analysis of the participation factors values in Table 1.

It can be concluded that the approximation of the Floquet modes as a finite number of Fourier components selected based on the participation factor should be able to describe the dynamical behavior of an LTP system as long as the minimum participation is low enough. In the next section, it will be proven that the approximation can be identified with a subspace method without modification.

2.5. Quantification of the approximation error

To wrap up the theoretical study, this approximation error will be quantified as a function of the minimum participation factor. Precisely, the error on the periodic amplitudes will be quantified. First, with $\hat{Y}_j(t)$ the

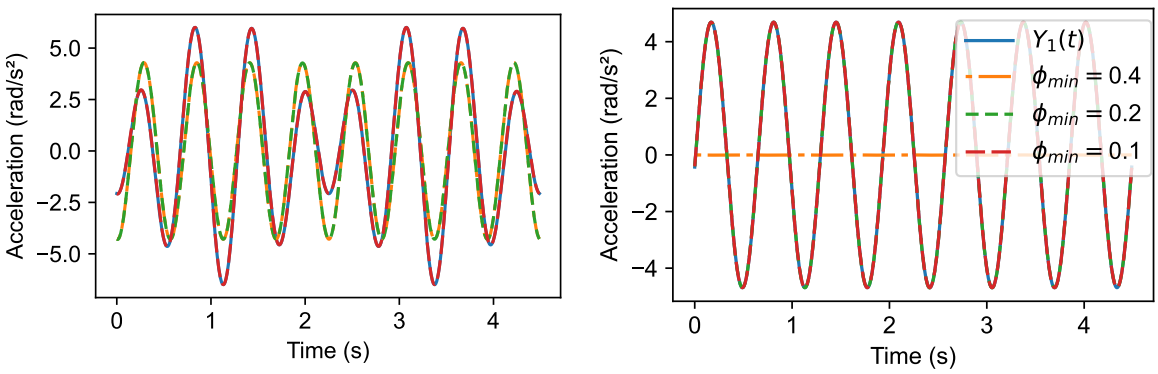

(a) Rotor

(b) Tower (Yaw)

Figure 2: Comparison over a period of the real part of the periodic mode shape of the reference Floquet model (continuous line) with different approximations (dashed lines) for different values of the minimum participation factor (ϕ_{min}) – First Floquet mode corresponding to the Yaw motion

approximation of the amplitude of the j–th Floquet mode, the Fourier series decomposition of the gap between the periodic amplitude and the approximation writes

$$Y_j(t) - \hat{Y}_j(t) = \sum_{l=-\infty}^{\infty} Y_{j,l} \exp(il\Omega t) - \sum_{l,\phi^y_{j,l} \geq \phi^y_{min}} Y_{j,l} \exp(il\Omega t) \tag{17}$$

$$= \sum_{l,\phi^y_{j,l} < \phi^y_{min}} Y_{j,l} \exp(il\Omega t), \tag{18}$$

With the identity of Parseval, it comes

$$\|Y_j(t) - \hat{Y}_j(t)\| = \frac{1}{T} \int_{-T/2}^{T/2} \|Y_j(t) - \hat{Y}_j(t)\|^2 dt = \sum_{l,\phi^y_{j,l} < \phi^y_{min}} \|Y_{j,l}\|^2. \tag{19}$$

With Equation (14)

$$\|Y_{j,l}\|^2 = \phi^y_{j,l} \sum_{k=-\infty}^{\infty} \|Y_{j,k}\|^2, \tag{20}$$

leading to

$$\|Y_j(t) - \hat{Y}_j(t)\| = \sum_{l,\phi^y_{j,l} < \phi^y_{min}} \phi^y_{j,l} \left(\sum_{k=-\infty}^{\infty} \|Y_{j,k}\|^2 \right). \tag{21}$$

Furthermore,

$$\sum_{l,\phi^y_{j,l} < \phi^y_{min}} \phi^y_{j,l} = 1 - \sum_{l,\phi^y_{j,l} \geq \phi^y_{min}} \phi^y_{j,l}, \tag{22}$$

as the sum of all the participation factors of a Floquet mode is 1. Consequently,

$$\|Y_j(t) - \hat{Y}_j(t)\| \leq \left(1 - \sum_{l,\phi^y_{j,l} \geq \phi^y_{min}} \phi^y_{j,l} \right) \sum_{k=-\infty}^{\infty} \|Y_{j,k}\|^2. \tag{23}$$

With the identity of Parseval $\sum_{k=-\infty}^{\infty} \|Y_{j,k}\|^2 = \|Y_j(t)\|$, so the second term of the previous equation is constant. Also,

$$\lim_{\phi^y_{min} \to 0} \sum_{l,\phi^y_{j,l} \geq \phi^y_{min}} \phi^y_{j,l} = 1, \tag{24}$$

so

$$\lim_{\phi^y_{min} \to 0} \|Y_j(t) - \hat{Y}_j(t)\| = 0, \ \forall \ j \in [1:n] \text{ and } t \in \mathbb{R}^+. \tag{25}$$

As a conclusion, the approximation error should tend to zero similarly to the minimum participation factor.

3. Subspace identification of the approximation

3.1. State-space expression of the approximation

The objective of this section is to express the state-space representation of the approximation. Once these matrices are defined, they can be inserted into the state-space defined for an LTP system (Equation (3)).

Equation (16) shows that the formulation of the observation $\hat{y}(t)$ corresponding to the approximation is similar to the formulation of the observation of an LTI system. So there must exist a state-space composed of some state vector $z(t) \in \mathbb{R}^{\tilde{n}}$, with the approximation of the observation $\hat{y}_h(t)$ of the homogeneous part,

$$\begin{cases} \dot{z}_h(t) = \tilde{A} z_h(t) \\ \hat{y}_h(t) = \tilde{C} z_h(t) \end{cases}, \tag{26}$$

with $\tilde{A}$ and $\tilde{C}$ the transition and observation matrices of the approximation and $z_h(t)$ of the form

$$z_h(t) = \sum_{p=1}^{\tilde{n}} Z_p \exp\left(\bar{\mu}_p t\right) q_p(0). \tag{27}$$

By injecting Equation (27) into Equation (26), it comes

$$\sum_{p=1}^{\tilde{n}} Z_p \bar{\mu}_p \exp\left(\bar{\mu}_p t\right) q_p(0) = \tilde{A} \sum_{p=1}^{\tilde{n}} Z_p \exp\left(\bar{\mu}_p t\right) q_p(0), \tag{28}$$

and by expressing the sums in matrix form

$$\mathcal{Z}\left[\bar{\mu}\right] \exp([\bar{\mu}]\, t) q(0) = \tilde{A} \mathcal{Z} \exp([\bar{\mu}]\, t) q(0), \tag{29}$$

with $\mathcal{Z} \in \mathbb{R}^{\tilde{n} \times \tilde{n}}$ regrouping the amplitudes of the state vector Z_p (one vector per column), $[\bar{\mu}]$ a diagonal matrix containing the eigenvalues of the approximation and $q(0) \in \mathbb{R}^{\tilde{n}}$ regrouping the scalar $q_p(0)$. So, the transition matrix is defined as

$$\tilde{A} = \mathcal{Z}\left[\bar{\mu}\right] \mathcal{Z}^{-1} \in \mathbb{R}^{\tilde{n} \times \tilde{n}}. \tag{30}$$

With $\tilde{C}$ the observation matrix of the approximation from Equation (26), and Equations (16) and (27), it comes

$$\sum_{p=1}^{\tilde{n}} Y_p \exp\left(\bar{\mu}_p t\right) q_p(0) = \tilde{C} \sum_{p=1}^{\tilde{n}} Z_p \exp\left(\bar{\mu}_p t\right) q_p(0). \tag{31}$$

Or, in a matrix form

$$\tilde{\Phi} \exp\left(\left[\bar{\mu}\right] t\right) q(0) = \tilde{C} \mathcal{Z} \exp\left(\left[\bar{\mu}\right] t\right) q(0) \tag{32}$$

with $\tilde{\Phi} \in \mathbb{R}^{r \times \tilde{n}}$ regrouping the amplitudes of the observed mode shapes. The observation matrix $\tilde{C}$ is expressed as

$$\tilde{C} = \tilde{\Phi} \mathcal{Z}^{-1} \in \mathbb{R}^{r \times \tilde{n}}. \tag{33}$$

To express the full discrete state-space, the discrete transition matrix and the input matrix are needed. First of all, let us define the observation of the state-space using Equation (4)

$$y(t) = C(t)\Phi(t)x(0) + C(t)\Phi(t) \int_0^t \Phi(\tau)^{-1} B_c(\tau) v(\tau) d\tau. \tag{34}$$

Using the approximation of the observation of the homogeneous part (Equation (16)) and Equations (32) , the approximation of $C(t)\Phi(t)$ is defined in matrix form

$$C(t)\Phi(t) \simeq \tilde{\Phi} \exp\left([\bar{\mu}]\, t\right) \tilde{\Psi}, \tag{35}$$

with $\tilde{\Psi}$ such that $q(0) = \tilde{\Psi} x(0)$. To express the approximation of $\Phi(\tau)^{-1}$, the approximation of the homogeneous part of the state-space is needed. With the same Fourier components as $\hat{y}_h(t)$

$$\hat{x}_h(t) = \sum_{p=1}^{\tilde{n}} X_p \exp\left(\bar{\mu}_p t\right) q_p(0), \tag{36}$$

leads to the approximation

$$\Phi(\tau) \simeq \mathcal{X} \exp\left([\bar{\mu}]\, \tau\right]) \tilde{\Psi}, \tag{37}$$

with $\mathcal{X} \in \mathbb{R}^{n \times \tilde{n}}$ regrouping the vectors X_p. For simplicity, if one assumes t a multiple of Δt, the approximation of the observation in discrete time is defined as

$$\hat{y}_k = \tilde{\Phi} \exp\left([\bar{\mu}]\, k\Delta t\right) q(0) + \tilde{\Phi} \exp\left([\bar{\mu}]\, k\Delta t\right) \sum_{i=1}^{k} I_i v_{i-1}, \tag{38}$$

with

$$I_i = \int_{(i-1)\Delta t}^{i\Delta t} \exp\left(-\left[\bar{\mu}_p\right] \tau\right) \mathcal{X}^{\dagger} B_c(\tau) d\tau, \tag{39}$$

where $(\cdot)^{\dagger}$ denotes the Moore-Penrose pseudo inverse and with the hypothesis of a zero-order hold on $v(t)$. With Equation (33), it is possible to express the observation matrix in $\hat{y}_{k+1}$ such that

$$\hat{y}_{k+1} = \tilde{C}\mathcal{Z} \exp\left([\bar{\mu}]\, (k+1)\Delta t\right) q(0) + \tilde{C}\mathcal{Z} \exp\left([\bar{\mu}]\, (k+1)\Delta t\right) \sum_{i=1}^{k+1} I_i v_{i-1}. \tag{40}$$

The state vector in discrete time z_k at time index $k+1$ is expressed as

$$z_{k+1} = \mathcal{Z} \exp\left([\bar{\mu}]\, (k+1)\Delta t\right) q(0) + \mathcal{Z} \exp\left([\bar{\mu}]\, (k+1)\Delta t\right) \sum_{i=1}^{k+1} I_i v_{i-1}. \tag{41}$$

Using the definition of z_k

$$z_{k+1} = \tilde{\mathbf{A}} z_k + \mathbf{B}_k v_k. \tag{42}$$

with $\tilde{\mathbf{A}} = \exp\left(\tilde{A}\Delta t\right)$ and $\mathbf{B}_k = \mathcal{Z} \exp\left([\bar{\mu}]\, (k+1)\Delta t\right) I_{k+1}$.

Finally, adding the term of the excitation in the observation leads to the discrete state-space of the approximation defined as

$$\begin{cases} z_{k+1} = \tilde{\mathbf{A}} z_k + \mathbf{B}_k v_k \\ \quad y_k = \tilde{\mathbf{C}} z_k + \mathbf{D}_k v_k + \tilde{w}_k \end{cases}, \tag{43}$$

with $\tilde{w}_k = w_k + \varepsilon_{y,\,k}$, where $\varepsilon_{y,\,k}$ is the approximation error of the observation (supposed to be with zero mean, independent with moments of same order as the noises). $\mathbf{B}_k$ and $\mathbf{D}_k = D(k\Delta t)$ are periodic matrices of period $T_d = \frac{T}{\Delta t}$. And $\tilde{C}$ is replaced by $\tilde{\mathbf{C}}$ for consistency. Assume $\tilde{\mathbf{A}}$ has all non zero distinct eigenvalues with modulus less than 1. Notice that a better modeling would be to include an additional input term u_k to the state equation to model the influence of external steady inputs to the system. Nonetheless, this u_k is assumed to be unmeasured, and it has been observed that output-only subspace identification techniques can identify those external nP as additional modes, see [13], having in mind here that the matrix $\tilde{\mathbf{A}}$ should be assumed of higher dimension to allow those modes to be estimated supplementary to the system modes.

Proof. let us prove the T_d periodicity of $\mathbf{B}_k$. Using Equations (38) and (39)

$$\mathbf{B}_k = \mathcal{Z} \exp\left([\bar{\mu}]\,(k+1)\Delta t\right) I_{k+1}. \tag{44}$$

Let us express $\mathbf{B}_{k+T_d}$, so

$$\mathbf{B}_{k+T_d} = \mathcal{Z} \exp\left([\bar{\mu}]\,(k+1)\Delta t\right) \exp\left([\bar{\mu}]\,T_d\Delta t\right) I_{k+T_d+1}, \tag{45}$$

moreover

$$I_{k+T_d+1} = \int_{(k+T_d)\Delta t}^{(k+T_d+1)\Delta t} \exp\left(-[\bar{\mu}]\,\tau\right) \mathcal{X}^\dagger B_c(\tau) d\tau \tag{46}$$

$$= \int_{(k)\Delta t}^{(k+1)\Delta t} \exp\left(-[\bar{\mu}]\,(\tau+T_d)\right) \mathcal{X}^\dagger B_c(\tau+T_d) d\tau. \tag{47}$$

But $B_c(\tau)$ is a periodic matrix, so $B_c(\tau+T_d) = B_c(\tau)\ \forall \tau \in \mathbb{R}^+$, thus

$$I_{k+T_d+1} = \exp\left(-[\bar{\mu}]\,T_d\Delta t\right) I_{k+1}. \tag{48}$$

Finally $\mathbf{B}_k = \mathbf{B}_{k+T_d}$ □

The state-space expression of the approximation has been defined, now it will be demonstrated that a subspace method can be used to identify the matrices $\tilde{\mathbf{A}}$ and $\tilde{\mathbf{C}}$, with first the definition of a subspace identification method.

3.2. Subspace identification of the approximation

Now that the state space representation has been defined (Equation (43)), it has to be proven that it can be identified with a classical subspace identification method. In this section, the Stochastic Subspace Identification (SSI) method [38] will be used, with the covariance-driven version. The first step in this method, is to construct a Hankel matrix filled by correlations, that can be constructed directly from matrices gathering the observations

$$\hat{H} = \mathcal{Y}^+ \left(\mathcal{Y}^-\right)^T. \tag{49}$$

Where $\mathcal{Y}^+ \in \mathbb{R}^{(p+1)r \times N}$ and $\mathcal{Y}^- \in \mathbb{R}^{qr \times N}$ such that

$$\mathcal{Y}^+ = \frac{1}{\sqrt{N}} \begin{bmatrix} y_{q+1} & y_{q+2} & \cdots & y_{q+N} \\ y_{q+2} & y_{q+3} & \cdots & y_{q+N+1} \\ \vdots & \vdots & \ddots & \vdots \\ y_{q+p+1} & y_{q+p+2} & \cdots & y_{q+p+N} \end{bmatrix} \text{ and } \mathcal{Y}^- = \frac{1}{\sqrt{N}} \begin{bmatrix} y_q & y_{q+1} & \cdots & y_{q+N-1} \\ y_{q-1} & y_q & \cdots & y_{q+N-2} \\ \vdots & \vdots & \ddots & \vdots \\ y_1 & y_2 & \cdots & y_N \end{bmatrix}. \tag{50}$$

Let us define the submatrices $\hat{H}_{m,n}$ of $\hat{H}$ by restriction to indices (m,n) $m \in [1:p+1]$ and $n \in [1:q]$ by

$$\hat{H}_{m,n} = \mathcal{Y}^+_m \left(\mathcal{Y}^-\right)^T_n, \tag{51}$$

with $\mathcal{Y}^+_m$ the m–th block line of $\mathcal{Y}^+$ and $(\mathcal{Y}^-)^T_n$ the n–th block column of $(\mathcal{Y}^-)^T$.

$$\begin{aligned} \mathcal{Y}^+_m &= \begin{bmatrix} y_{q+m} & y_{q+m+1} & \cdots & y_{q+N+m-1} \end{bmatrix} \\ \left(\mathcal{Y}^-\right)^T_n &= \begin{bmatrix} y^T_{q+1-n} & y^T_{q+2-n} & \cdots & y^T_{q+N+1-n} \end{bmatrix}^T \end{aligned} \tag{52}$$

Consequently, similarly to the LTI case

$$\hat{H}_{m,n} = \tilde{\mathbf{C}} \tilde{\mathbf{A}}^{m+n-2} \hat{G}_n + o(1), \tag{53}$$

based on the expression in Appendix A, where $o(1)$ a matrix converging to zero with N, with the demonstration developed in Appendix C. Then with $k_n = q+1-n+k$

$$\hat{G}_n(N) = \frac{1}{N}\sum_{k=0}^{N-1} \tilde{\mathbf{A}} z_{k_n} z_{k_n}^T \tilde{\mathbf{C}}^T + \mathbf{B}_{k_n} v_{k_n} v_{k_n}^T \mathbf{D}_{k_n}^T. \tag{54}$$

Firstly, assume that N is a multiple of T_d,

$$\hat{G}_n(N) = \frac{1}{N}\tilde{\mathbf{A}} \sum_{k=0}^{N-1} \left[z_{k_n} z_{k_n}^T\right] \tilde{\mathbf{C}}^T + \frac{1}{T_d}\sum_{j=1}^{T_d} \mathbf{B}_j \frac{T_d}{N} \sum_{\tilde{k}_j} \left[v_{\tilde{k}_j} v_{\tilde{k}_j}^T\right] \mathbf{D}_j^T, \tag{55}$$

where $\tilde{k}_j$ denote the indices corresponding to the specific instants of the period and where $\mathbf{B}_j$ and $\mathbf{D}_j$ are periodic matrices. Let us demonstrate that $\hat{G}_n$ and $\hat{H}_n$ converge.

Let $l \in [1; T_d[$ an integer, the matrix $\hat{G}_n$ estimated with $N+l$ data is defined as

$$\hat{G}_n(N+l) = \frac{1}{N+l}\tilde{\mathbf{A}} \sum_{k=0}^{N+l-1} \left[z_{k_n} z_{k_n}^T\right] \tilde{\mathbf{C}}^T + \frac{1}{T_d}\sum_{j=1}^{T_d} \mathbf{B}_j \frac{T_d}{N+l} \sum_{\tilde{k}_j} \left[v_{\tilde{k}_j} v_{\tilde{k}_j}^T\right] \mathbf{D}_j^T + \frac{1}{N+l}\sum_{k=N}^{N+l-1} \mathbf{B}_{k_n} v_{k_n} v_{k_n}^T \mathbf{D}_{k_n}^T. \tag{56}$$

The input and feedthrough matrices are bounded finite matrices and v_k is bounded in moments, $\sup_{k\geq 0} \mathbb{E}\left(\|\mathbf{B}_k v_k v_k^T \mathbf{D}_k\|^2\right) \leq C < \infty$. So, using the Chebyshev inequality and the Borel-Cantelli lemma

$$\lim_{N\to\infty} \frac{1}{N+l}\sum_{k=N}^{N+l-1} \mathbf{B}_{k_n} v_{k_n} v_{k_n}^T \mathbf{D}_{k_n}^T = 0, \tag{57}$$

also

$$\lim_{N\to\infty} \frac{1}{T_d}\sum_{j=1}^{T_d} \mathbf{B}_j \frac{T_d}{N+l} \sum_{\tilde{k}_j} \left[v_{\tilde{k}_j} v_{\tilde{k}_j}^T\right] \mathbf{D}_j^T = \lim_{N\to\infty} \frac{1}{T_d}\sum_{j=1}^{T_d} \mathbf{B}_j \frac{T_d}{N} \sum_{\tilde{k}_j} \left[v_{\tilde{k}_j} v_{\tilde{k}_j}^T\right] \mathbf{D}_j^T. \tag{58}$$

In Appendix B it is proven that $\frac{1}{N}\tilde{\mathbf{A}} \sum_{k=0}^{N-1} \left[z_{k_n} z_{k_n}^T\right] \tilde{\mathbf{C}}^T$ converges to a unique limit. Consequently, $\hat{G}_n(N)$ converges.

Let us express $\hat{G}_{n+1}(N)$. $\hat{G}_{n+1}(N)$ is $\hat{G}_n(N)$ shifted to the past. Precisely, $\hat{G}_n(N)$ is defined with the index from $q+1-n$ to $q+N+1-n$ while $\hat{G}_{n+1}(N)$ is defined with the index from $q-n$ to $q+N-n$. So, $\hat{G}_{n+1}(N)$ can be expressed as a function of $\hat{G}_n(N)$

$$\hat{G}_{n+1}(N) - \hat{G}_n(N) = \frac{1}{N}\sum_{k=0}^{N-1} \tilde{\mathbf{A}} z_{k_{n+1}} z_{k_{n+1}}^T \tilde{\mathbf{C}}^T + \mathbf{B}_{k_{n+1}} v_{k_{n+1}} v_{k_{n+1}}^T \mathbf{D}_{k_{n+1}}^T - \frac{1}{N}\sum_{k=0}^{N-1} \tilde{\mathbf{A}} z_{k_n} z_{k_n}^T \tilde{\mathbf{C}}^T + \mathbf{B}_{k_n} v_{k_n} v_{k_n}^T \mathbf{D}_{k_n}^T \tag{59}$$

In Appendix B, it has been proven that the initial index had no impact on the limit of the first term, consequently

$$\hat{G}_{n+1}(N) - \hat{G}_n(N) = \frac{1}{N}\left(\mathbf{B}_{q+N+1-n} v_{q+N+1-n} v_{q+N+1-n}^T \mathbf{D}_{q+N+1-n}^T - \mathbf{B}_{q-n} v_{q-n} v_{q-n}^T \mathbf{D}_{q-n}^T\right) \tag{60}$$

$\sup_{k\geq 0} \mathbb{E}\left(\|\mathbf{B}_k v_k v_k^T \mathbf{D}_k^T\|^2\right) \leq C < \infty$, finally, using the Chebyshev inequality and the Borel-Cantelli lemma

$$\lim_{N\to\infty} \left(\hat{G}_{n+1}(N) - \hat{G}_n(N)\right) = 0. \tag{61}$$

Analogously for all i and all n such that $1 \leq n < n+i \leq q$, $\lim_{N\to\infty} \left(\hat{G}_{n+i}(N) - \hat{G}_n(N)\right) = 0$. Finally, $\lim_{N\to\infty} \hat{G}_n(N) = G$ is invariant regarding the index n.

From the previous result, the matrix $\hat{H}$ can be expressed term by term as

$$\lim_{N\to\infty} \hat{H} = \begin{bmatrix} \tilde{\mathbf{C}}G & \tilde{\mathbf{C}}\tilde{\mathbf{A}}G & \dots & \tilde{\mathbf{C}}\tilde{\mathbf{A}}^{q-1}G \\ \tilde{\mathbf{C}}\tilde{\mathbf{A}}G & \tilde{\mathbf{C}}\tilde{\mathbf{A}}^{2}G & \dots & \tilde{\mathbf{C}}\tilde{\mathbf{A}}^{q}G \\ \vdots & \vdots & \ddots & \vdots \\ \tilde{\mathbf{C}}\tilde{\mathbf{A}}^{p}G & \tilde{\mathbf{C}}\tilde{\mathbf{A}}^{p+1}G & \dots & \tilde{\mathbf{C}}\tilde{\mathbf{A}}^{p+q-1}G \end{bmatrix}. \tag{62}$$

The Hankel matrix can be factorized such that $\hat{H} = O_p C_q$, where O_p denotes the observability matrix and C_q the controllability matrix,

$$O_p = \begin{bmatrix} \tilde{\mathbf{C}} \\ \tilde{\mathbf{C}}\tilde{\mathbf{A}} \\ \vdots \\ \tilde{\mathbf{C}}\tilde{\mathbf{A}}^{p} \end{bmatrix} \quad \text{and} \quad C_q = \begin{bmatrix} G & \tilde{\mathbf{A}}G & \dots & \tilde{\mathbf{A}}^{q-1}G \end{bmatrix}. \tag{63}$$

The observability matrix and the controlability matrix are somewhat similar to those derived under the usual LTI assumptions (see [38]). Thus, the approximation of an LTP system can be estimated with the SSI method. Also, it implies that the computation of Gaussian confidence intervals is possible, similarly to [24].

Similarly, as for the LTI case, O_p is full column rank and C_q is full row rank. The observability matrix is obtained from a thin singular value decomposition of $\hat{H}$ and its truncation at the correct model order $\tilde{n}$

$$\hat{H} = U\Sigma V^T = \begin{bmatrix} U_1 & U_2 \end{bmatrix} \begin{bmatrix} \Sigma_1 & 0 \\ 0 & \Sigma_2 \end{bmatrix} \begin{bmatrix} V_1^T \\ V_2^T \end{bmatrix}, \tag{64}$$

$$O_p = U_1 \Sigma_1^{1/2}, \tag{65}$$

where Σ_1 contains the first n singular values and U_1 the n first column of U. The observation matrix $\tilde{\mathbf{C}}$ is identified as the first block row of O_p and the state transition matrix $\tilde{\mathbf{A}}$ is identified in a least-squares sense

$$O_{p\ (2:p+1)} = O_{p\ (1:p)} \tilde{\mathbf{A}}, \tag{66}$$

with $O_{p\ (1:p)}$ the first p blocks rows of O_p and $O_{p\ (2:p+1)}$ the p last blocks rows. Then, the modes can be computed with the eigenvalue decomposition of $\tilde{\mathbf{A}}$, namely $\tilde{\mathbf{A}} = \Psi \left[\tilde{\lambda}_i\right] \Psi^{-1}$. The continuous time eigenvalues $\tilde{\mu}_i$ are deduced from the discrete time eigenvalues $\tilde{\lambda}_i$ by $\tilde{\mu}_i = \log(\tilde{\lambda}_i)/\Delta t$. Then the natural frequency (f_i) and the damping (ζ_i) of the associated mode are defined such that $f_i = |\tilde{\mu}_i|/2\pi$ and $\zeta_i = -100 \times \Re(\tilde{\mu}_i)/|\tilde{\mu}_i|$. Finally, the observed mode shape matrix is found from $\tilde{\Phi} = \tilde{\mathbf{C}}\Psi$.

Notice that the model truncation requires the introduction of a threshold when dealing with the modeling in Section 2 to discard the Fourier components of small participation. This truncation is implicitly obtained without user interaction or definition of an empirical threshold by using the classical SSI approach without modification when analyzing data since there is an equivalence between the discarded model Fourier components and the modes that are non identified by the SSI approach.

In this section we have shown that the LTP system can be approximated by an LTI system under periodic inputs where the corresponding LTI modes can be related to the Fourier components of the LTP Floquet modes. Precisely, it has been proved that the classical system identification and uncertainty estimation developed for

LTI systems where all $(\tilde{\mathbf{A}}, \tilde{\mathbf{B}}, \tilde{\mathbf{C}}, \tilde{\mathbf{D}})$ matrices are assumed to be constant can be applied directly to estimate this particular LTI model - which approximate the original LTP model, despite that the input and feedthrough matrices, $\tilde{\mathbf{B}}$ and $\tilde{\mathbf{D}}$, are periodic.

In the following, the uncertainty estimation will be tested and validated for the identification of the approximation of an LTP system using an identification of the 5DOF wind turbine model.

3.3. Validation of the uncertainty quantification method

In the previous section, it was demonstrated that the uncertainty estimation method for LTI systems can be used in addition to the corresponding system identification for LTI systems as a meaningful features collection of the LTP dynamics in some approximated sense. A numerical validation of such claim is now developed. Considering the uncertainty computation, following [23, 24], the method estimates the covariance matrices of the identified modes from the same data used for the subspace covariance-driven identification. From the covariance matrices, it is possible to express the standard deviations σ_f and σ_ζ of the frequency and damping. To perform the uncertainty quantification, a first order approximation is used. Thus, using the sensitivity matrix of the considered parameter regarding the correlations and the covariance matrices of correlations $(\hat{\Sigma}_R)$, the covariance matrix of all the identified parameters can be estimated. For example, the covariance matrix of an eigenfrequency is

$$\hat{\text{cov}}(f_i) = \mathcal{J}_{f_i} \hat{\Sigma}_R \mathcal{J}_{f_i}^T. \tag{67}$$

Where $\mathcal{J}_{f_i}$ denotes the sensitivity of the i–th eigenfrequency regarding the correlations, with $\mathcal{J}_{f_i} = \frac{\partial f_i}{\partial \text{vec}(R)}$. The sensitivity of the frequencies, damping and mode shapes of the modes are defined in [10].

In this example, a Monte Carlo simulation is performed on the 5DOF wind turbine model to compare the estimated uncertainties with the empirical uncertainties. The Monte Carlo simulation is composed of 2000 independent identifications used as a reference estimation of the uncertainties. The simulation input is generated with the same Gaussian covariance for each run. The generated data are sampled at 25 Hz during 600s. For each run of the Monte Carlo simulation, the identification of the wind turbine parameters is performed at model order (18) and with the same lag parameters (q+1=p=100). Finally, the empirical uncertainties from the Monte Carlo simulation are compared with the mean estimated uncertainties from 100 other identifications (referred as the estimation in the following (est)), where σ_f denotes the standard deviation of the frequency and σ_ζ denotes the standard deviation of the damping.

The comparison of the estimated and empirical standard deviations for all the modes with a frequency between 0.4 Hz and 2 Hz is reported in Table 2. Table 2 shows that the estimated and the empirical standard deviations are close, with all the empirical standard deviations inside the confidence interval of the estimated standard deviations. Those results are similar to those described in [24], consequently, the uncertainty quantification method can also be used as a companion for the LTI identification of the approximation of an LTP system.

The next section will be dedicated to the application of the identification of an LTP system approximation, with the identification of a realistic model of wind turbine.

4. Application : identification of a multi-physic model of wind turbine

In this section, an identification of an aero-servo-elastic wind turbine numerical model is performed, then compared with the modal dynamics as extracted from a Floquet analysis of the same turbine.

Frequency (Hz)	$\sigma_{f\ MC}$ (Hz)	$\sigma_{f\ est}$ (Hz)	Damping (%)	$\sigma_{\zeta\ MC}$ (%)	$\sigma_{\zeta\ est}$ (%)
0.448	4.11×10^{-3}	$3.26 \pm 2.34\times10^{-3}$	0.344	0.376	0.580 ± 0.408
0.641	8.60×10^{-4}	$8.60 \pm 7.00\times10^{-4}$	0.324	0.145	0.129 ± 0.068
0.670	7.40×10^{-4}	$7.20 \pm 4.20\times10^{-4}$	0.230	0.118	0.100 ± 0.058
0.746	8.10×10^{-4}	$7.20 \pm 3.80\times10^{-4}$	0.267	0.116	0.099 ± 0.05
0.864	8.90×10^{-4}	$1.00 \pm 1.62\times10^{-3}$	0.240	0.115	0.124 ± 0.23
1.087	1.14×10^{-3}	$1.91 \pm 2.66\times10^{-3}$	0.191	0.119	0.171 ± 0.26
1.248	2.60×10^{-3}	$2.80 \pm 1.96\times10^{-3}$	0.936	0.195	0.227 ± 0.204
1.367	2.75×10^{-3}	$3.44 \pm 3.84\times10^{-3}$	0.794	0.190	0.295 ± 0.66
1.470	3.13×10^{-3}	$4.59 \pm 6.10\times10^{-3}$	0.794	0.202	0.310 ± 0.416
1.590	3.06×10^{-3}	$5.87 \pm 7.48\times10^{-3}$	0.682	0.176	0.344 ± 0.422
1.693	3.94×10^{-3}	$7.00 \pm 8.76\times10^{-3}$	0.690	0.203	0.467 ± 0.968
1.813	6.53×10^{-3}	$8.27 \pm 9.82\times10^{-3}$	0.598	0.269	0.593 ± 1.218

Table 2: Comparison of the empirical standard deviation ($\sigma._{MC}$) and the estimated standard deviation ($\sigma._{est}$) of the frequency and damping with the empirical 95% uncertainty bound

Notice that the term LTI modes (or simply modes) will be used preferably when discussing about the estimates of the Fourier components through the SSI method.

Precisely, the DTU 10MW wind turbine is considered [3, 36], implemented within the software OpenFAST [20]. The turbine is placed in a turbulent wind generated with the software TurbSim [17], with a mean speed of 7 m/s and a class A IEC turbulence (with a turbulence intensity of 24%), using the Kaimal turbulence model. It has been decided to simulate wind conditions with a high turbulence level to validate the identification of the LTI modes of a rotating wind turbine on a challenging example. The rotational speed of the turbine is controlled by an external controller [15]. In this section, the rotor configuration is assumed to be isotropic (i.e. all blades have the same features) and the effects of gravity are taken into account. So, the system is not isotropic, but the MBC transform can be used to compute the Floquet modes of the wind turbine model. The Fourier components coming from both the MBC method and Floquet theory have been empirically compared and are very close. Time-marching simulations throughout 600 s are then calculated, allowing to extract "synthetic sensor" vibration time-series.

This realistic wind turbine model deviates from the assumptions made in Section 2 in two aspects at least: the system is theoretically no longer linear, nor periodic because of the turbulent wind (see Figure 3 where the joint evolution of the wind speed and turbine rotation speed is reported), the identification result is then expected to estimate a mean structural state corresponding to the mean rotational speed over the signal. Moreover, the excitation is no longer white noise (see [33] for a discussion). It is therefore interesting to see to what extent the algorithms can nevertheless achieve a satisfactory identification.

In this paper, the vocabulary commonly used in wind energy is used. *Side-Side* and *Fore-Aft* denote the tower bending in and out of the rotor plane, respectively. *Edge* and *Flap* denote the blades bending in and out of the rotor plane, respectively. Different blade modes have to be considered depending on their relative phases. For example, for the edge and flap modes, the collective edge represents the in-phase bending of the blades; the backward and forward edge whirl correspond to out of phase ($\pm120°$) bending of the blades. For the backward edge Floquet mode, the bending of the second blade is delayed compared to the first blade. For the forward edge Floquet mode, the bending of the second blade is in advance compared to the bending of the first blade. These two bending modes of frequency f_{edge} have an impact on the tower with two different LTI modes, with, due to

low damping, a frequency of $f_{edge} - \frac{\Omega}{2\pi}$ and $f_{edge} + \frac{\Omega}{2\pi}$, respectively, where Ω denotes the rotational speed of the rotor. Consequently, the frequencies of the LTI modes corresponding to the backward and Forward edge Floquet modes estimated using sensors situated on the tower have a gap of Ω/π.

4.1. Computation of model modes using Floquet analysis

For isotropic rotors, it has been shown by Skjoldan [29] that Floquet modes can be recovered from an MBC analysis. This strategy has thus been adopted here. Setting a constant rotation speed of 6 rpm for the turbine (corresponding to the average rotational speed, see Figure 3), it is possible to compute a periodic steady-state solution with OpenFAST, about which MBC modes are computed using the method of Bir [6]. A minimum participation factor of 5% is applied in (14) to obtain the truncated Floquet modal basis. Fore-Aft (FA) and Side-Side (SS) accelerations of the mid-tower and tower top, and the flap and edge blade root bending moments are used to compute the participation factor. It can be noted that the minimum participation factor for this model is lower than the one used for the 5DOF wind turbine model. This is because the threshold is chosen such that the sum of the participation factors for each Floquet mode is close to 1 and that all non negligible Fourier components are selected.

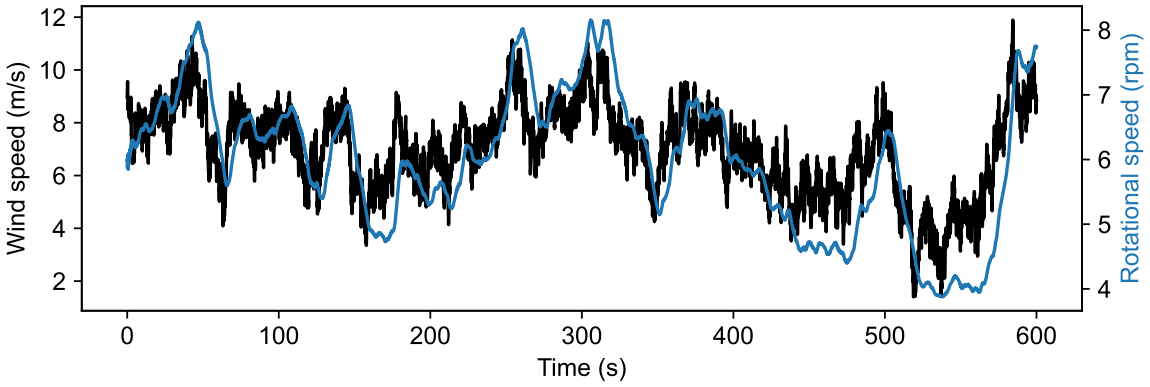

Figure 3: Evolution of the wind speed and the rotational speed during the simulation

The modal frequencies calculated from the model can be compared with power spectral densities (PSD) extracted from the time-domain simulations. Specifically, in Figure 4, PSDs for a blade root edge bending moment (red curve) and a side-side tower acceleration (blue curve) are reported. On top of these PSDs, the frequencies of some LTI modes of the model approximation are added, namely the two first Side-Side bending LTI modes of the tower and the LTI modes of the three different Floquet modes of edge bending (backward, forward, and collective). The type of mode is found by visualizing the mode shape. It can be seen that frequency peaks in PSDs are matching well with the frequencies of the model LTI modes. The only peak that is not matching with the approximation is the peak corresponding to the effect of gravity coupled with the rotation of the rotor and the misalignment of the wind with the shaft. This peak is called the *1P* with a frequency of $\frac{\Omega}{2\pi}$=0.1 Hz in this example. This indicates that an LTP modeling of the system seems to be appropriate, despite the fact that the "true" model is not LTP, because the rotational speed is not constant. Also notice that the SSI method has estimated the *1P* as a zero-damped LTI mode, as predicted by [13].

Furthermore, the modal truncation based on participation factor allows to select all modes relevant to describe the dynamics of the system while discarding negligible components. As it was said in Section 2, the position and

the number of sensors influence the number of non negligible Fourier components identifiable in the signal and then the approximate LTI model to be identified. Here, we select the sensors as the tower accelerations and the blade root moments.

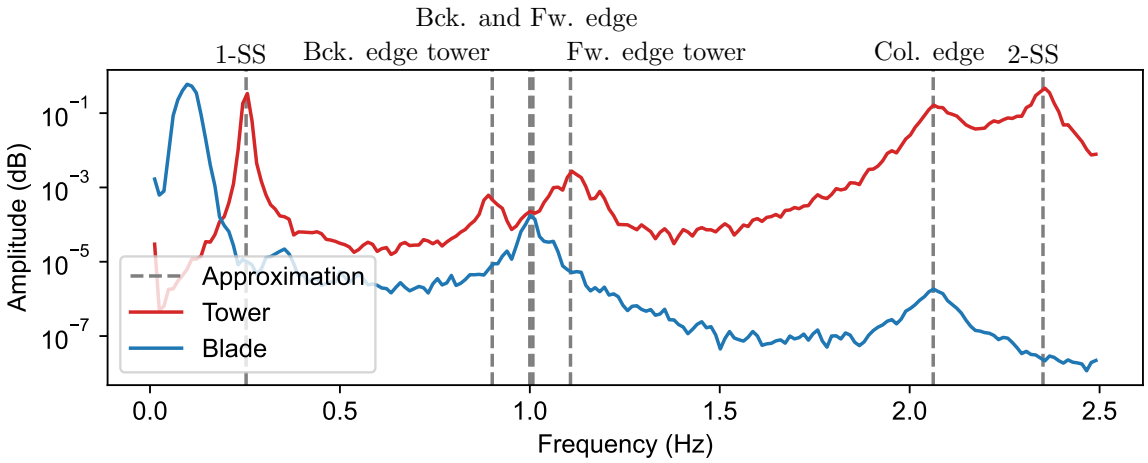

Figure 4: Normalized PSD of of a blade edge bending DOF and a tower Side-Side DOF compared to the frequencies of relevant model LTI modes (dashed lines and names)

In the next section, a subspace identification with uncertainty quantification will be performed on the synthetic sensor time-series data. To complete the validation, the identified modes will eventually be compared with the model LTI modes (which represent "ground-truth" results in this case).

4.2. Subspace Identification of the DTU wind turbine

In this section, the identification of the DTU 10 MW wind turbine modal properties is performed using simulated time-series of blade root bending moments and tower accelerations together.

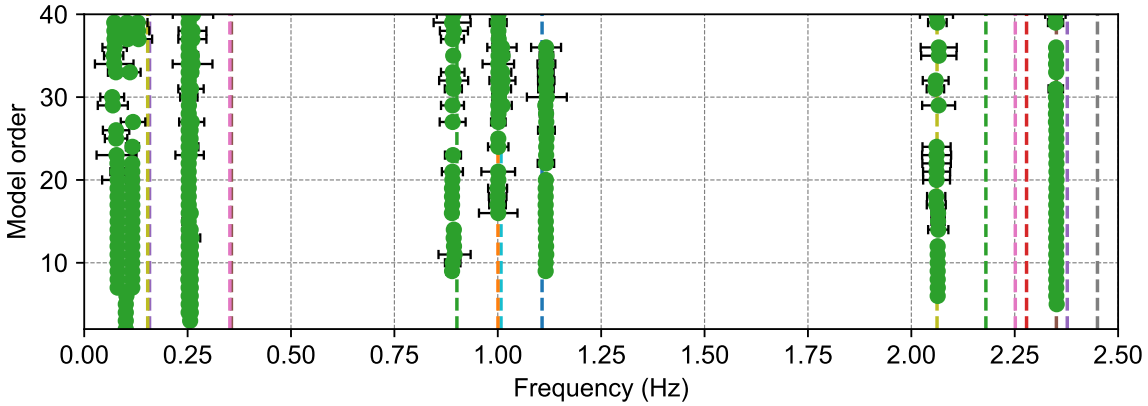

Figure 5: Stabilization diagram from an identification with all the data, from a simulation with a turbulent wind and a variable rotational speed - (- - -): model LTI modes frequencies - (•): identified frequencies - error bars at the 95% confidence interval

The identified modes are displayed in Figure 5 using a stabilization diagram, where the frequencies of the identified LTI modes are displayed in regards to the model order assumed in the identification. Also, the uncertainty quantification method defined in [10] has been used as a way to filter the results (only modes with a low uncertainty are kept, as they are more likely to correspond to physical modes).

	f_{ap} (Hz)	f_{iden} (Hz)	σ_f (Hz)	ζ_{ap} (%)	ζ_{iden} (%)	σ_ζ (%)	MAC	Names
Tower	2.351	2.351	0.003	0.869	0.987	0.124	1.000	2-SS
	2.062	2.064	0.006	1.778	1.732	0.280	1.000	Col. edge
	1.107	1.116	0.004	2.066	2.715	0.436	0.907	Fw. edge tower
	0.901	0.892	0.006	1.908	2.252	0.274	0.975	Bck. edge tower
	0.257	0.258	0.004	7.776	7.502	1.204	0.998	1-FA
	0.253	0.253	0.001	0.275	0.352	0.277	0.744	1-SS
Rotor	2.062	2.064	0.006	1.778	1.732	0.280	0.969	Col. edge
	1.008	1.010	0.011	2.269	1.771	1.184	0.759	Fw. edge rotor
	1.000	1.001	0.005	1.719	1.792	0.417	0.915	Bck. edge rotor
	0.257	0.258	0.004	7.776	7.502	1.204	0.983	1-FA

Table 3: Summary of the identification results, with the matching of the identified modes with the LTI modes

It can be seen in Figure 5, that the modes observed in the PSD are identified, also another mode has been identified (the first Fore-Aft bending at 0.25Hz). Moreover, the *1P* can be seen once again, with identified modes of frequency around 0.1Hz. Once the modes are identified and selected, they are matched with the model LTI modes using the Modal Assurance Criterion (MAC) [22].

$$\mathrm{MAC}(\phi_{iden}, Y_{j,l}) = \frac{\left|\phi_{iden}^H Y_{j,l}\right|^2}{\left(\phi_{iden}^H \phi_{iden}\right)\left(Y_{j,l}^H Y_{j,l}\right)}, \tag{68}$$

with ϕ_{iden} the mode shape of an identified (from data) mode and $Y_{j,l}$ the l–th amplitude of Fourier of the j–th Floquet mode (from model, see Equation (15)). The modes are matched twice, once using only the tower DOF, and once using only the rotor DOF. Eight modes are identified, whose frequencies and damping (mean over several orders) are reported in Table 3 in columns f_{iden} and ξ_{iden} respectively. These values are compared with the frequencies and damping of the LTI modes obtained from the approximated model of the Floquet modes of the OpenFAST model (Section 4.1), indicated in columns f_{ap} and ξ_{ap} respectively. A very good agreement is observed: the relative gap between the identified modes from the data and the model LTI modes is lower than 1%, which is acceptable considering the uncertainties of the identified modes (σ_f and σ_ζ). Some model LTI modes, like the mode 2-FA and the flap bending modes, are not identified due to their high damping ratios (more than 30% for the flap bending modes and around 13% for the mode 2-FA). Those non-identified modes are not observed in the PSDs (Figure 4).

To show that the LTI modes derived from the Floquet modes have been well identified, the example of the backward edge mode will be used. First, let us consider the periodic mode shape and the participation factor of the Fourier components (computed in Section 4.1). Figure 6(a,b) shows the evolution of the periodic mode shape over a rotation at different tower and rotor DOFs. It can be seen that the periodic mode shape of the backward edge mode has only two non negligible components (Figure 6c). Looking at the identification results (Table 3, Bck. edge tower and Bck. edge rotor), it can be seen that the LTI modes of those two Fourier components have been identified. It can be concluded that all LTI modes of the backward edge Floquet mode are well identified in this example.

In Figure 7, the full unnormalized mode shapes at a fixed azimuth angle of the two Fourier components are displayed. It is important to remember that the mode shapes of the wind turbine are coupled with the rotation of the rotor. The corresponding LTI mode shapes are identified through the accelerations of the tower and the blade root moment. Both model and identified LTI mode shapes match with MAC values over 0.9. It implies

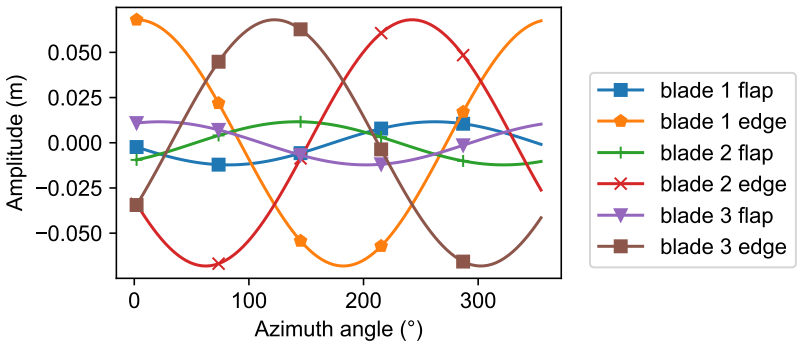

(a) Evolution of the periodic mode shape on the rotor DOF

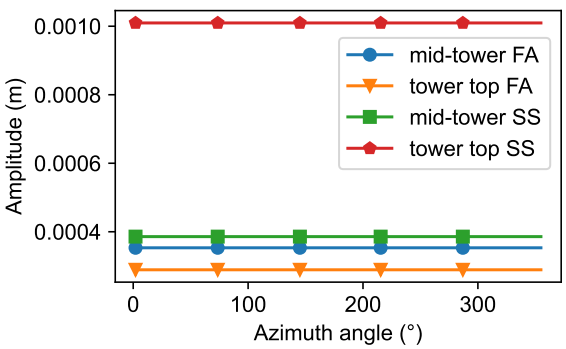

(b) Evolution of the periodic mode shape on the tower DOF

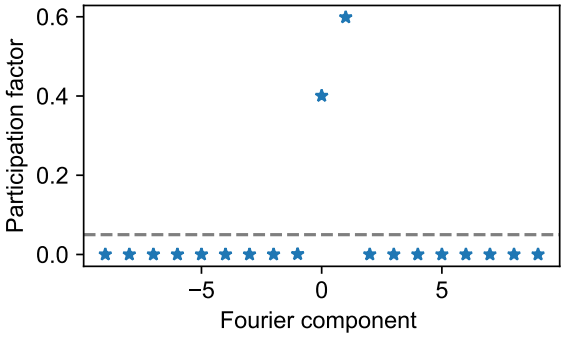

(c) Participation factors, with the minimum participation factor represented by the dashed line

Figure 6: Periodic mode shape of the backward edge Floquet mode

that the identified modes obtained with the current formalism are close to those numerically predicted with the approximation, with data dynamics realistically close to real measurements.

Notice that the uncertainty of the identified modes is dependent on the turbulence intensity. Our simulated example exhibits a relatively high turbulence level. A lower intensity for the turbulence would yield to lower uncertainties for the modal estimates. The simulated example shows the efficiency of the estimation despite a rather high turbulence intensity.

Now, it will be shown that the identification of the approximation can be used to perform fault detection, with an application of the detection of a stiffness reduction of a blade, through the monitoring of the rotor anisotropy.

5. Impact of the anisotropy on the Floquet modes and introduction of reliable features to track for structural fault detection

The main interest in monitoring wind turbines is to detect the occurrence of faults in the structure to ensure effective maintenance. For this purpose, reliable and fault-sensitive features have to be determined. So before performing an identification, the impact of a stiffness drop of a blade on the model LTI modes will be assessed. To assess a change in the model LTI modes, the approximation of the DTU 10MW wind turbine model is computed for three different global stiffness reductions of the third blade, namely 1%, 2.5% and 5%. Here, the Floquet modes are computed from an integration of the homogeneous equation (see Section 2.2).

First, the change in the frequencies of the LTI modes will be assessed. In Table 4, the evolution of the natural frequencies of different model LTI modes is summarised depending on the stiffness loss of the damaged blade. In this example, all the values have been computed for a rotational speed of 6 rpm. Looking at the results, one can

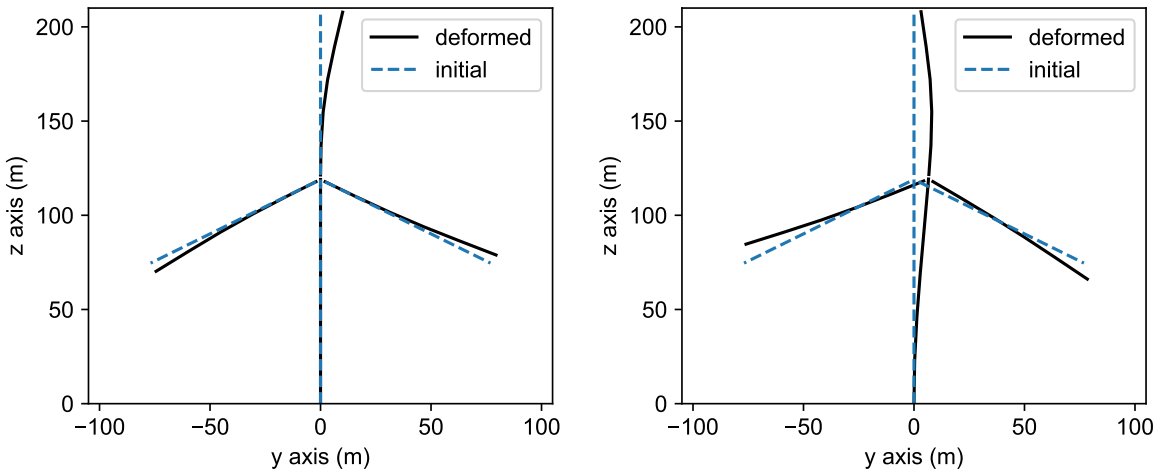

(a) f=1.000 Hz, h=1

(b) f=0.901 Hz, h=0

Figure 7: Unnormalized mode shapes of the LTI modes of the backward edge Floquet mode, at a fixed azimuth angle

see that whatever the loss in stiffness is, the frequency change remains negligible. Indeed, the difference between the natural frequencies between the two structural states is negligible, with a maximum of 0.015 Hz of difference for the collective edge. This order of magnitude is not significant enough to track such change in a real structure, where the effects of varying environmental conditions will be important [11]. Consequently, the frequency cannot be used as a reliable indicator to detect changes in the rotor properties. So, another approach is investigated and the change in the mode shapes due to the anisotropy will be assessed, as it is introduced in [9, 32].

Name	Isotropic	99% of stiff.	97.5% of stiff.	95% of stiff.
2-SS	2.349	2.348	2.348	2.348
Col. Edge	2.061	2.058	2.054	2.046
Fw. Tower	1.108	1.107	1.106	1.105
Fw. Rotor	1.008	1.007	1.006	1.005
Bck. Tower	0.901	0.899	0.896	0.888
1-FA	0.257	0.257	0.257	0.257
1-SS	0.253	0.253	0.253	0.253

Table 4: Some frequencies of the LTI modes as a function of the stiffness for the third blade

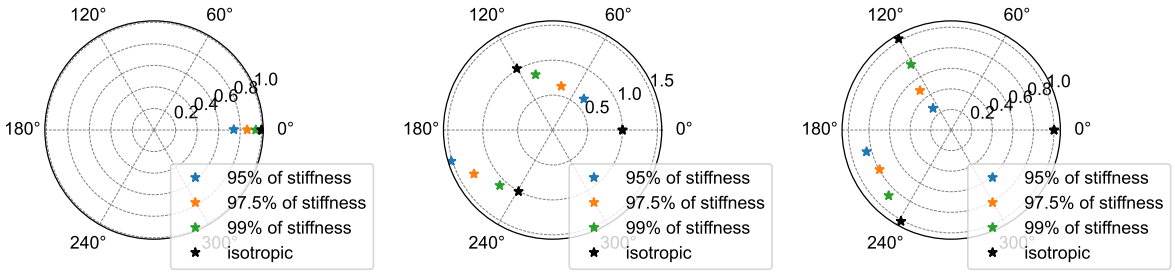

(a) Collective

(b) Backward

(c) Forward

Figure 8: Evolution of the polar plot of the edgewise bending mode shapes against the third blade stiffness

Figure 8 represents the evolution of the amplitude and the phase shift between the blades on a polar plot for the different considered stiffness reductions, where each subfigure corresponds to a different mode. First, it has to be noted that the first blade defines the reference, with an amplitude always equal to 1 and a phase to 0.

The choice of the reference blade will have an impact on the values of phase shift and amplitude, but the global change compared to the isotropic state is the same. Figures 8b and 8c show that there is an important evolution of the phase shift for the backward and forward edge bending modes coupled with an important evolution of their amplitude. Indeed, for the isotropic state, the phase shift between each blade is 120° and the amplitude is equal to 1 for each blade. For a stiffness loss of 5%, the phase shift decreases to about 50° and 190° for the 2nd and 3rd blades for the backward edge bending mode respectively, whereas the vibration amplitude decreases for the 2nd blade and increases for the third one. Considering the forward edge bending mode, the amplitudes for each blade decrease, but it decreases substantially for the 2nd blade (to about 0.2). The phase shift of the second blade remains somewhat constant and equal to 120°, whereas it decreases for the third blade. The collective edge has a different evolution compared to the two others. Indeed, only the amplitude of the damaged blade is evolving with a reduction of the amplitude according to the loss of stiffness. These results illustrate the high sensitivity of the phase shift and amplitude to a rotor anisotropy and the relevance of tracking these parameters to monitor a wind turbine.

Mode	Stiff. 99%	Stiff. 97.5%	Stiff. 95%
Col.	0.999	0.996	0.982
Bck.	0.968	0.846	0.691
Fw.	0.973	0.849	0.704

Table 5: MAC criterion of the whirling mode, computed between the isotropic and the anisotropic modes for different anisotropy levels

Table 5 summarizes the MAC between the mode shapes of the isotropic state and the anisotropic states. It confirms the graphical analysis as a larger evolution of the MAC is observed for the backward and forward edge mode shapes. It can be concluded that the mode shapes of the backward and the forward edge have a similar sensitivity to anisotropy. The mode shape of the collective edge is less affected globally by the change scenarios since only the amplitude of the damaged blade is affected by the rotor anisotropy.

Another feature reactive to anisotropy is the appearance of new Fourier components, corresponding to new identified modes. However, this feature will not be used, since it reveals only the presence of high rotor anisotropy.

In conclusion, due to the important sensitivity of the mode shapes of the edge bending modes regarding the anisotropy, the mode shapes can be used to detect the anisotropy. In the next section, the anisotropy detection method will be exposed and validated with an example of the detection of a global stiffness drop of 5% and a local stiffness drop of a blade.

6. Anisotropy detection method

As the identified modes are obtained from correlation estimates, they are uncertain. Consequently, to compare the phase shift and the amplitude obtained with different identifications, the identified values, and the associated uncertainties have to be compared. The next section is dedicated to the algorithmic development of the uncertainty computation for the phase shift and the amplitude.

6.1. Definition: Sensitivity of phase shift and amplitude

With the uncertainty computation method presented in Section 3.3, the uncertainties are estimated with the first-order delta method. So, from the covariance matrix of a mode shape, it is possible to estimate the

uncertainties of the associated phase shift and amplitude, with the sensitivity matrices of each parameter with respect to the mode shape. To do so, those sensitivity matrices will be defined.

First, let us define the phase shift p_j of a mode shape $\phi \in \mathbb{R}^r$ at DOF j. The mode shape at the DOF j can be defined as

$$\phi_j = a_j \exp(ip_j) = a_j \cos(p_j) + ia_j \sin(p_j), \tag{69}$$

where a_j denotes the amplitude. From this expression, the phase shift can be defined as

$$p_j = \operatorname{atan2}(\Im(\phi_j), \Re(\phi_j)). \tag{70}$$

So, the sensitivity of the phase shift regarding the mode shape is defined as

$$\mathcal{J}_{P,\phi} = \begin{bmatrix} \frac{\partial P}{\partial \Re(\phi)} & \frac{\partial P}{\partial \Im(\phi)} \end{bmatrix} \in \mathbb{R}^{r \times 2r}. \tag{71}$$

First

$$\frac{\partial p_j}{\partial \Re(\phi_j)} = -\frac{\Im(\phi_j)}{\Re(\phi_j)^2} \frac{1}{1 + \left(\frac{\Im(\phi_j)}{\Re(\phi_j)}\right)^2} = \frac{-\Im(\phi_j)}{|\phi_j|^2}, \tag{72}$$

analogously

$$\frac{\partial p_j}{\partial \Im(\phi_j)} = \frac{1}{\Re(\phi_j)} \frac{1}{1 + \left(\frac{\Im(\phi_j)}{\Re(\phi_j)}\right)^2} = \frac{\Re(\phi_j)}{|\phi_j|^2}. \tag{73}$$

Finally, the definition of $\mathcal{J}_{P,\phi}$ is

$$\mathcal{J}_{P,\phi} = \begin{bmatrix} \begin{bmatrix} \frac{-\Im(\phi_k)}{|\phi_k|^2} \end{bmatrix} & \begin{bmatrix} \frac{\Re(\phi_k)}{|\phi_k|^2} \end{bmatrix} \end{bmatrix}, \tag{74}$$

with $\begin{bmatrix} \frac{\Im(-\phi_k)}{|\phi_k|^2} \end{bmatrix} \in \mathbb{R}^{r \times r}$ a diagonal matrix, as for $\begin{bmatrix} \frac{\Re(\phi_k)}{|\phi_k|^2} \end{bmatrix}$. $\mathcal{J}_{P,\phi}$ is defined and non-zero if ϕ is non-zero for all degrees of freedom. This condition is verified if the associated mode shape is non zero at every sensor. If a mode shape has a zero amplitude at a sensor, it is not useful to estimate the phase shift and its uncertainty.

The amplitude (a_i) of the DOF i of the mode shape ϕ is defined as

$$a_i = |\phi_i| = \sqrt{\Re(\phi_i)^2 + \Im(\phi_i)^2}. \tag{75}$$

Analogously as previously, the sensitivity of the amplitude regarding the mode shape has to be defined,

$$\mathcal{J}_{a,\phi} = \begin{bmatrix} \frac{\partial a}{\partial \Re(\phi)} & \frac{\partial a}{\partial \Im(\phi)} \end{bmatrix} \in \mathbb{R}^{r \times 2r}. \tag{76}$$

With

$$\frac{\partial a_i}{\partial \Re(\phi_i)} = \frac{\Re(\phi_i)}{|\phi_i|} \text{ and } \frac{\partial a_i}{\partial \Im(\phi_i)} = \frac{\Im(\phi_i)}{|\phi_i|}, \tag{77}$$

the sensitivity matrix ($\mathcal{J}_{a,\phi}$) is defined as

$$\mathcal{J}_{a,\phi} = \begin{bmatrix} \begin{bmatrix} \frac{\Re(\phi_k)}{|\phi_k|} \end{bmatrix} & \begin{bmatrix} \frac{\Im(\phi_k)}{|\phi_k|} \end{bmatrix} \end{bmatrix}. \tag{78}$$

Where $\begin{bmatrix} \frac{\Re(\phi_k)}{|\phi_k|} \end{bmatrix} \in \mathbb{R}^{r \times r}$ is a diagonal matrix, as for $\begin{bmatrix} \frac{\Im(\phi_k)}{|\phi_k|} \end{bmatrix}$. Like $\mathcal{J}_{P,\phi}$, $\mathcal{J}_{a,\phi}$ is defined and non-zero if ϕ is non-zero for all sensors.

So, the uncertainties of the phase shift and the amplitude can be defined using the sensitivity matrices. Now the identification and the uncertainty computation methods will be used to monitor the change of the identified edgewise bending mode shapes with the analysis of the phase shift and the amplitude, to detect anisotropy.

6.2. Method to detect rotor anisotropy

As told in the previous section, the identified modes obtained are uncertain. Thus, to determine if a mode shape has changed, it is necessary to compare the identified values taking into account the associated uncertainties. The MAC criterion can be used to determine if two mode shapes are statistically distinct. In [14], it has been shown that the MAC follows different statistical laws depending on the compared mode shapes. If the compared mode shapes are identical, the criterion follows a χ^2 law and if the mode shapes are different, it follows a Gaussian law. For the χ^2 law, the confidence interval is defined with the lower bound of the 95% quantile as the upper bound is 1. For the Gaussian law, the confidence interval is computed based on the standard deviation.

The objective of the method is to assess changes in the mode shapes. To achieve such a goal, an actual set of identified modes has to be compared to a reference set. Precisely, a change in the rotor isotropy is sought through changes in the edgewise bending modes. The method to detect anisotropy changes is composed of the following steps:

1. Identification of the reference state using only the blade root edge-moment: uncertainty computation of the reference mode shape, amplitude and phase shift
2. Identification of the current state (potentially damaged) using only the blade root edge-moment: uncertainty computation of the current mode shape, amplitude and phase shift
3. Comparison of the edgewise bending mode shape and their associated uncertainties on a polar plot. The compared estimated mode shapes are not corresponding to the same state if the 95% confidence intervals do not cross each other
4. Computation of the MAC criterion and the associated uncertainties. If the MAC follows a χ^2 law, the mode shapes correspond to the same state, whereas if the MAC follows a Gaussian law the mode shapes are corresponding to different states and anisotropy is detected.

Now, this method will be tested, with a change scenario in the DTU 10MW rotor isotropy.

6.3. Detection of a 5% global loss of stiffness under turbulent wind

In this example, a global loss of 5% of stiffness on the third blade is simulated for the damaged state. To have the same environmental conditions, both states (reference and damaged) are simulated with the same turbulent wind used in Section 4, sampled at 25Hz during 600s.

In Figures 9a, 9b and 9c, the mode shapes of the three edge bending modes can be compared. These figures represent the phase shift and the amplitudes of the three blades with their uncertainty intervals for the three different modes considered. As it was stated in Section 5, the first blade defines the reference, so the associated phase and amplitude to this blade are exact (without uncertainty). In Figures 9a and 9b, the confidence intervals of the reference and damaged states do not cross each other. It can be concluded, that the associated mode shapes are different for the backward and collective edge. In Figure 9c, the confidence intervals are crossing each other, so the corresponding mode shapes cannot be considered different. Now, this graphical analysis will be validated, with the study of the statistical law of the MAC.

Table 6 summarizes the MAC and uncertainties of each mode. For the collective and backward edge, the value of the identified MAC is below the lower bounds of the 95% quantile defined with a chi-square law modeling. This confirms that the mode shapes of the damaged state are different from those of the reference state. Also,

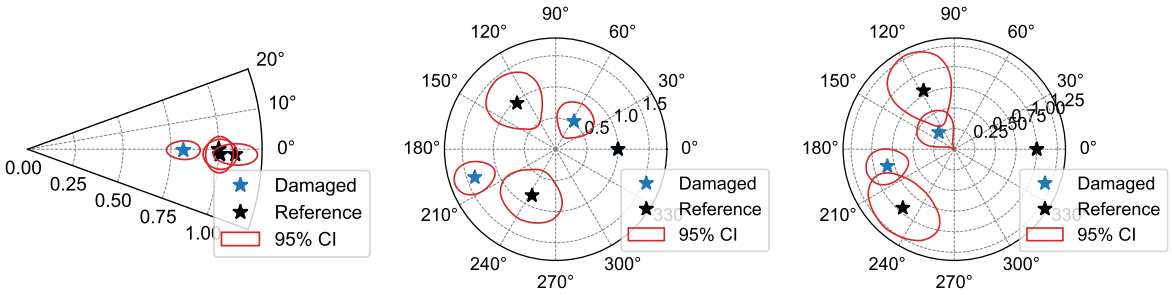

(a) Collective (b) Backward (c) Forward

Figure 9: Comparison of the edgewise bending mode shapes between the reference and the damaged states, for a global stiffness drop of 5%

Name	MAC	Standard deviation	Quantile
Col.	0.983	0.009	0.991
Bck.	0.667	0.157	0.786
Fw.	0.806	0.152	0.684

Table 6: MAC criterion and the respective uncertainties, global stiffness drop of 5%

the MAC of the forward edge mode may follow a chi-square law, meaning that the mode shapes can not be discriminated. Consequently, the uncertainty analysis for the MAC is validating the graphical analysis based on the confidence interval.

The confidence interval in Figure 9 are estimated. To validate these estimations, they can be compared with the results of a Monte Carlo simulation. Here the phase shift and amplitude of the edgewise bending modes are computed from 100 simulations of the isotropic rotor and 100 simulations of the damaged rotor. Then the empirical confidence intervals can be computed.

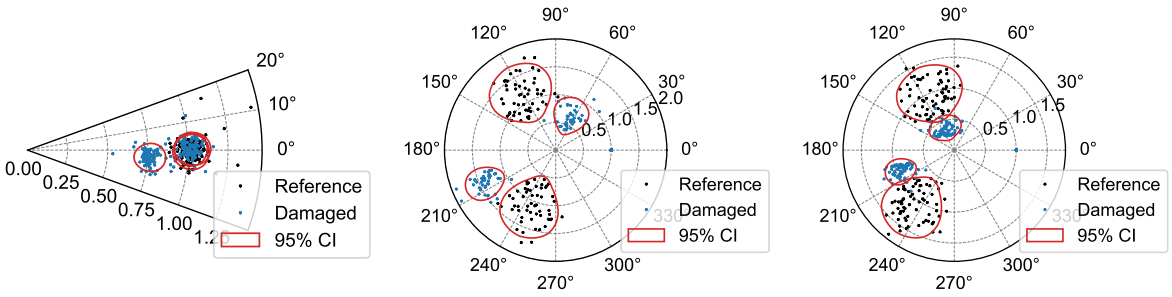

(a) Collective (b) Backward (c) Forward

Figure 10: Comparison of the edgewise bending mode shapes between the reference and the damaged states for 100 identifications of both states, for a global stiffness drop of 5%

In Figure 10, the edgewise bending mode shapes are displayed with polar plots for the 100 identifications of the reference and damaged structure. Based on these, the 95% confidence intervals can be computed. Compared to the estimated ones (Figure 9), it can be concluded that the confidence intervals are similar. Consequently, it validates the estimation of the uncertainties of the phase shift and amplitude of the identified mode shapes.

6.4. Detection of a local loss of stiffness

Finally, the method can be tested with a simulation of a more realistic damage, with a local loss of stiffness. More precisely, the damage is modelled as a loss of 20% of stiffness in the first five elements of the blade (the

closest to the blade root), corresponding to 10% of the total length. Where this local damage has a similar impact on the LTI modes compared to the global loss of stiffness of 5%. The reference case is the same as in the previous section and the damaged case is computed from a simulation with the same wind speed as previous simulations.

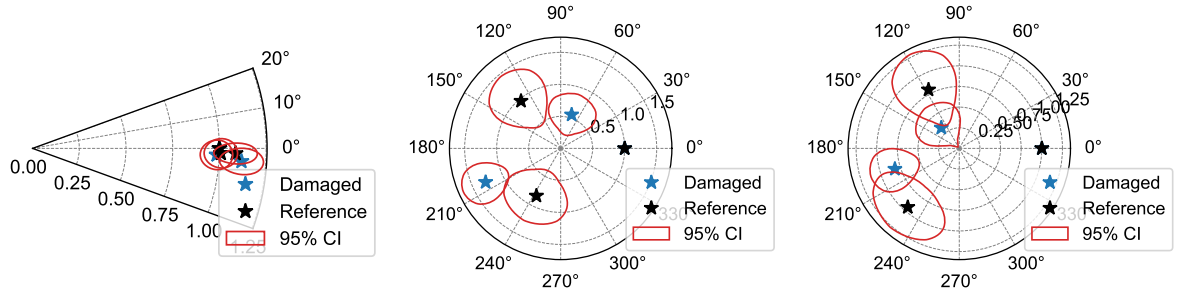

(a) Collective

(b) Backward

(c) Forward

Figure 11: Comparison of the edgewise bending mode shapes between the reference and the damaged states, for a local stiffness drop of 20%

Name	MAC	Standard deviation	Quantile
Col.	0.999	0.002	0.992
Bck.	0.740	0.156	0.770
Fw.	0.843	0.145	0.665

Table 7: MAC criterion and the respective uncertainties, local stiffness drop of 20%

Similarly, Figure 11 regroups the results from the identification and the uncertainty bounds of the phase shift and mode amplitude for the three edge bending modes. It can be seen that the confidence intervals are overlapping each other, except for the backward edge (Figure 11b). So, only the mode shape of the backward has changed enough. Besides, with the uncertainties of the MAC (Table 7), the MAC of the different mode shapes of the collective and the forward edge are following a χ^2 law, meaning that they are statistically identical. Once again, the MAC criterion confirms the graphical study of the confidence intervals.

In conclusion, with this method, it is also possible to detect a local loss of stiffness. To detect smaller damage, a guideline is to increase the length of the measurements to reduce the covariance of the identified parameters. Nonetheless, there is an expected trade off between the system stationarity (better with short signals) and the method accuracy (better with long signals).

7. Conclusion

It has been shown that the dynamical behavior of an LTP system can be described as an LTI system under inputs with periodic moments resulting from an approximation of the LTP Floquet modes. Also, it has been proven that the classical output-only identification methods and the associated uncertainty computation methods can be used without modification for the identification of LTI modes of the approximation. Those LTI modes correspond to the identifiable Fourier components of the Floquet modes from the LTP system. Then, the interest and efficiency of the modeling are demonstrated on an aero-servo-elastic model of a 10 MW wind turbine. Finally, it has been shown that the relative amplitude and phase of the mode shape of the first LTI edge bending modes, namely the backward, forward and collective edge, are good indicators of rotor anisotropy. So, based on the new

development of an uncertainty scheme for those indicators, a method to monitor the change of those quantities has been defined and tested on simulated data. Regarding the results, it can be concluded that the analysis of the edgewise bending mode shapes can be used for fault detection and in general that the LTI modes can be used for the monitoring of wind turbines. It has to be noted that using this Fourier decomposition modeling implies losing the relation between the identified LTI modes and the physical LTP model. If this relation is needed, which is not the case for the introduced anisotropy method in Section 6, then other identification methods of the literature - as described in the introduction - should be preferred. Combining the advantage of approaches defined for the approximate LTI model and the exact LTP model should be envisaged in further works. Another possible extension is to take into account the external loads such as the nP into the modeling following the ideas of [37, 13].

Acknowledgments

Jean Charlety is acknowledged for his comments and advice.

Appendix A. Proof of Equation (53)

Let $k_m = q + m + k$ and $k_n = q + 1 - n + k$ with $k_m = k_n + m + n - 1$, with Equation (52) it yields

$$\hat{H}_{m,n} = \frac{1}{N}\sum_{k=0}^{N-1}\left(\tilde{\mathbf{C}}z_{k_m} + \mathbf{D}_{k_m}v_{k_m} + \tilde{w}_{k_m}\right)\left(\tilde{\mathbf{C}}z_{k_n} + \mathbf{D}_{k_n}v_{k_n} + \tilde{w}_{k_n}\right)^T. \tag{A.1}$$

Let us define z_{k_m} function of z_{k_n}

$$z_{k_m} = \tilde{\mathbf{A}}^{m+n-1}z_{k_n} + \sum_{j=1}^{m+n-1}\tilde{\mathbf{A}}^{j-1}\mathbf{B}_{k_m-j}v_{k_m-j}. \tag{A.2}$$

From this expression, the submatrix of the Hankel matrix can be defined as

$$\begin{aligned}
\hat{H}_{m,n} = {} & \tilde{\mathbf{C}}\tilde{\mathbf{A}}^{m+n-2}\frac{1}{N}\sum_{k=0}^{N-1}\left(\tilde{\mathbf{A}}z_{k_n}z_{k_n}^T\tilde{\mathbf{C}}^T + \tilde{\mathbf{A}}z_{k_n}v_{k_n}^T\mathbf{D}_{k_n}^T + \tilde{\mathbf{A}}z_{k_n}\tilde{w}_{k_n}^T\right) \\
& + \tilde{\mathbf{C}}\tilde{\mathbf{A}}^{m+n-2}\frac{1}{N}\sum_{k=0}^{N-1}\left(\mathbf{B}_{k_n}v_{k_n}z_{k_n}^T\tilde{\mathbf{C}}^T + \mathbf{B}_{k_n}v_{k_n}v_{k_n}^T\mathbf{D}_{k_n}^T + \mathbf{B}_{k_n}v_{k_n}\tilde{w}_{k_n}^T\right) \\
& + \frac{1}{N}\sum_{k=0}^{N-1}\sum_{j=1}^{m+n-2}\tilde{\mathbf{C}}\tilde{\mathbf{A}}^{j-1}\left(\mathbf{B}_{k_m-j}v_{k_m-j}z_{k_n}^T\tilde{\mathbf{C}}^T + \mathbf{B}_{k_m-j}v_{k_m-j}v_{k_n}^T\mathbf{D}_{k_n}^T + \mathbf{B}_{k_m-j}v_{k_m-j}\tilde{w}_{k_n}^T\right) \\
& + \frac{1}{N}\sum_{k=0}^{N-1}\left(\mathbf{D}_{k_m}v_{k_m}z_{k_n}^T\tilde{\mathbf{C}}^T + \mathbf{D}_{k_m}v_{k_m}v_{k_n}^T\mathbf{D}_{k_n}^T + \mathbf{D}_{k_m}v_{k_m}\tilde{w}_{k_n}^T\right) \\
& + \frac{1}{N}\sum_{k=0}^{N-1}\left(\tilde{w}_{k_m}z_{k_n}^T\tilde{\mathbf{C}}^T + \tilde{w}_{k_m}v_{k_n}^T\mathbf{D}_{k_n}^T + \tilde{w}_{k_m}\tilde{w}_{k_n}^T\right).
\end{aligned} \tag{A.3}$$

Appendix B. Proof of the convergence of $\frac{1}{N}\sum_{k=0}^{N} z_k z_k^T$

Let us express the state vector at the index $k + T_d$ as a function of the inputs and the state vector at the index k,

$$z_{k+T_d} = \tilde{\mathbf{A}}^{T_d}z_k + \sum_{j=1}^{T_d}\tilde{\mathbf{A}}^{j-1}\mathbf{B}_{k+j-1}v_{k+j-1}. \tag{B.1}$$

Let us define the extended state vector

$$Z_k = \begin{bmatrix} z_k^T & z_{k+1}^T & \dots & z_{k+T_d-1}^T \end{bmatrix}^T \in \mathbb{R}^{\tilde{n}T_d}, \tag{B.2}$$

also the extended input vector can be defined as

$$V_k = \begin{bmatrix} v_k^T & v_{k+1}^T & \dots & v_{k+T_d-1}^T \end{bmatrix}^T \in \mathbb{R}^{mT_d}. \tag{B.3}$$

Using Equation (B.1) for any index a

$$Z_{a+T_d} = \mathbb{A}Z_a + \mathbb{B}V_a, \tag{B.4}$$

with

$$\mathbb{A} = \begin{bmatrix} \tilde{\mathbf{A}}^{T_d} & 0 & \dots & 0 \\ 0 & \tilde{\mathbf{A}}^{T_d} & \dots & 0 \\ \vdots & \vdots & \ddots & \vdots \\ 0 & \dots & & \tilde{\mathbf{A}}^{T_d} \end{bmatrix} \text{ and } \mathbb{B} = \begin{bmatrix} \tilde{A}^{T_d-1}\mathbf{B}_a & \tilde{A}^{T_d-2}\mathbf{B}_{a+1} & \dots & \mathbf{B}_{a+T_d-1} \\ \tilde{A}^{T_d-1}\mathbf{B}_{a+1} & \tilde{A}^{T_d-2}\mathbf{B}_{a+2} & \dots & \mathbf{B}_a \\ \vdots & \vdots & \ddots & \vdots \\ \tilde{A}^{T_d-1}\mathbf{B}_{a+T_d-1} & \tilde{A}^{T_d-2}\mathbf{B}_a & \dots & \mathbf{B}_{a+T_d-2} \end{bmatrix}. \tag{B.5}$$

From Equation (B.4), it is possible to express an LTI relation

$$Z_{K+1} = \mathbb{A}Z_K + \mathbb{B}V_K, \tag{B.6}$$

where

$$Z_K = \begin{bmatrix} z_{a+KT_d}^T & z_{a+KT_d+1}^T & \dots & z_{a+KT_d+T_d-1}^T \end{bmatrix}^T, \tag{B.7}$$

and similarly for V_K. Also in other words the new index K denotes the period index and a the initial index in the vector Z_0. Equation (B.6) defines an LTI system of size $\tilde{n}T_d$ where the matrix $\mathbb{B}$ had a lines arrangement depending of a, thus,

$$\lim_{\tilde{N}\to\infty} \frac{1}{\tilde{N}} \sum_{K=0}^{\tilde{N}} Z_K Z_K^T = \mathbb{E}\left(Z_K Z_K^T\right). \tag{B.8}$$

To prove that $\frac{1}{N}\sum_{k=0}^{N} z_k z_k^T$ converges, Equation (B.8) will be used. First,

$$Z_K Z_k^T = \sum_{l=0}^{T_d-1} z_{a+KT_d+l} z_{a+KT_d+l}^T. \tag{B.9}$$

Consequently,

$$\frac{1}{\tilde{N}} \sum_{K=0}^{\tilde{N}} Z_k Z_k^T = \frac{1}{\tilde{N}} \sum_{K=0}^{\tilde{N}} \sum_{l=0}^{T_d-1} z_{a+KT_d+l} z_{a+KT_d+l}^T \tag{B.10}$$

$$= T_d \frac{1}{N} \sum_{k=0}^{N} z_{a+k} z_{a+k}^T, \text{ with } N = T_d\tilde{N}, \tag{B.11}$$

as $\frac{1}{\tilde{N}}\sum_{K=0}^{\tilde{N}} Z_k Z_k^T$ converges, $\frac{1}{N}\sum_{k=0}^{N} z_{a+k} z_{a+k}^T$ also converges. Now let us prove that it converges to the same limit $\forall a > 0$. Let us define $a' \neq a$, so

$$\frac{1}{N}\sum_{k=0}^{N} z_{a+k} z_{a+k}^T - \frac{1}{N}\sum_{k=0}^{N} z_{a'+k} z_{a'+k}^T = \begin{cases} \frac{1}{N}\left(\sum_{k=N+a'}^{N+a} z_k z_k^T - \sum_{k=a'}^{a} z_k z_k^T\right), & a > a' \\ \frac{1}{N}\left(-\sum_{k=N+a}^{N+a'} z_k z_k^T + \sum_{k=a}^{a'} z_k z_k^T\right), & a < a' \end{cases}. \tag{B.12}$$

$\sup_{k\geq 0}\mathbb{E}\left(\|z_k z_k^T\|^2\right) \leq C < \infty$, consequently, using the Chebyshev inequality and the Borel-Cantelli lemma

$$\lim_{N\to\infty}\left(\frac{1}{N}\sum_{k=0}^{N} z_{a+k}z_{a+k}^T - \frac{1}{N}\sum_{k=0}^{N} z_{a'+k}z_{a'+k}^T\right) = 0 \tag{B.13}$$

Finally, $\frac{1}{N}\sum_{k=0}^{N} z_{a+k}z_{a+k}^T$ converges to the same limit $\forall a \geq 0$.

Appendix C. Proof of the convergence in $o(1)$

First using Equation (A.3)

$$S_{m,n}(N) = \hat{H}_{m,n} - \tilde{\mathbf{C}}\tilde{\mathbf{A}}^{m+n-2}\frac{1}{N}\sum_{k=0}^{N-1}\left(\tilde{\mathbf{A}}z_{k_n}z_{k_n}^T\tilde{\mathbf{C}}^T + \mathbf{B}_{k_n}v_{k_n}v_{k_n}^T\mathbf{D}_{k_n}^T\right) \tag{C.1}$$

let us prove the convergence to zero of all parts of $S_{m,n}(N)$, using Lemma 3 of [4]. $S_{m,n}(N)$ can be separated as follows

$$S_{m,n}(N) = S_{m,n\ z}(N) + S_{m,n\ v}(N) + S_{m,n\ vB}(N) + S_{m,n\ vD}(N) + S_{m,n\ w}(N). \tag{C.2}$$

First

$$S_{m,n\ v}(N) = \tilde{\mathbf{C}}\tilde{\mathbf{A}}^{m+n-2}\frac{1}{N}\sum_{k=0}^{N-1}\left(\mathbf{B}_{k_n}v_{k_n}z_{k_n}^T\tilde{\mathbf{C}}^T + \mathbf{B}_{k_n}v_{k_n}\tilde{w}_{k_n}^T\right) \tag{C.3}$$

Assuming N is a multiple of T_d, similarly to (56)

$$S_{m,n\ v}(N) = \tilde{\mathbf{C}}\tilde{\mathbf{A}}^{m+n-2}\frac{1}{T_d}\sum_{l=1}^{T_d}\mathbf{B}_l\frac{T_d}{N}\sum_{k_l}\left(v_{k_l}z_{k_l}^T\tilde{C}^T + v_{k_l}\tilde{w}_{k_l}^T\right), \tag{C.4}$$

where k_l denotes the indices at the same discrete time l in the period. Expressing z_{k_l} function of z_{k_l-1}

$$S_{m,n\ v}(N) = \tilde{\mathbf{C}}\tilde{\mathbf{A}}^{m+n-2}\frac{1}{T_d}\sum_{l=1}^{T_d}\mathbf{B}_l\frac{T_d}{N}\sum_{k_l}\left(v_{k_l}z_{k_l-1}^T\tilde{\mathbf{A}}^T\tilde{\mathbf{C}}^T + v_{k_l}v_{k_l-1}^T\mathbf{B}_{l-1}\tilde{\mathbf{C}}^T + v_{k_l}\tilde{w}_{k_l}^T\right). \tag{C.5}$$

v_{k_l} and z_{k_l} are square integrable random variables such that $\sup_{k\geq 0}\mathbb{E}\left(v_{k_l}v_{k_l}^T\right) \leq C < \infty$ and $\lim_{N\to\infty}\frac{1}{N}\sum_{k_l}\|z_{k_l}\|^2 \leq C < \infty$ (proof in Appendix B). Also, they are $\mathcal{Y}_k$-measurable and $\mathbb{E}\left(v_k|\mathcal{Y}_{k-1}\right) = 0$, where $\mathcal{Y}_{k-1}$ denotes the family of variables y_0 to y_{k-1}. So using Lemma 3 of [4]

$$\lim_{N\to\infty}\tilde{\mathbf{C}}\tilde{\mathbf{A}}^{m+n-2}\frac{1}{T_d}\sum_{l=1}^{T_d}\mathbf{B}_l\frac{T_d}{N}\sum_{k_l}v_{k_l}z_{k_l-1}^T\tilde{\mathbf{A}}^T\tilde{\mathbf{C}}^T = 0. \tag{C.6}$$

v_k is a Gaussian white noise, so it is a sequence of independent variables with zero mean

$$\lim_{N\to\infty}\tilde{\mathbf{C}}\tilde{\mathbf{A}}^{m+n-2}\frac{1}{T_d}\sum_{l=1}^{T_d}\mathbf{B}_l\frac{T_d}{N}\sum_{k_l}v_{k_l}v_{k_l-1}^T\mathbf{B}_{l-1}\tilde{\mathbf{C}}^T + v_{k_l}\tilde{w}_{k_l}^T = 0. \tag{C.7}$$

Finally, leading to

$$\lim_{N\to\infty}S_{m,n\ v}(N) = 0. \tag{C.8}$$

Secondly, following the same steps as above,

$$S_{m,n\ vB}(N) = \frac{1}{N}\sum_{k=0}^{N-1}\sum_{j=1}^{m+n-2}\tilde{\mathbf{C}}\tilde{\mathbf{A}}^{j-1}\left(\mathbf{B}_{k_m-j}v_{k_m-j}z_{k_n}^T\tilde{\mathbf{C}}^T + \mathbf{B}_{k_m-j}v_{k_m-j}v_{k_n}^T\mathbf{D}_{k_n}^T + \mathbf{B}_{k_m-j}v_{k_m-j}\tilde{w}_{k_n}^T\right). \tag{C.9}$$

Leading to

$$S_{m,n\ vB}(N) = \frac{1}{N}\sum_{j=1}^{m+n-2}\sum_{k=0}^{N-1}\tilde{\mathbf{C}}\tilde{\mathbf{A}}^{j-1}\left(\tilde{v}_{k_m-j}z_{k_n}^T\tilde{\mathbf{C}}^T + \tilde{v}_{k_m-j}v_{k_n}^T\mathbf{D}_{k_n}^T + \tilde{v}_{k_m-j}\tilde{w}_{k_n}^T\right), \tag{C.10}$$

where $\mathbf{B}_k v_k = \tilde{v}_k$. z_{k_n} and $\tilde{v}_k$ are square integrable variables such that $\sup_{k\geq 0}\mathbb{E}\left(\tilde{v}_k\tilde{v}_k^T\right) \leq C < \infty$ and $\lim_{N\to\infty}\frac{1}{N}\sum_{k_l}\|z_{k_l}\|^2 \leq C < \infty$. Also they are $\mathcal{Y}_k$-measurable and $\mathbb{E}\left(\tilde{v}_k|\mathcal{Y}_{k-1}\right) = 0$. $k_m - j > k_n$ for $1 < j < m+n-2$, so using Lemma 3 of [4]

$$\lim_{N\to\infty}\frac{1}{N}\sum_{j=1}^{m+n-2}\sum_{k=0}^{N-1}\tilde{\mathbf{C}}\tilde{\mathbf{A}}^{j-1}\left(\tilde{v}_{k_m-j}z_{k_n}^T\tilde{\mathbf{C}}^T\right) = 0. \tag{C.11}$$

v_k and $\tilde{w}_k$ are independent Gaussian process, so

$$\lim_{N\to\infty} S_{m,n\ vB}(N) = 0. \tag{C.12}$$

Following with $S_{m,n\ vD}(N)$,

$$S_{m,n\ vD}(N) = \frac{1}{N}\sum_{k=0}^{N-1}\left(\bar{v}_{k_m}z_{k_n}^T\tilde{\mathbf{C}}^T + \bar{v}_{k_m}v_{k_n}^T\mathbf{D}_{k_n}^T + \bar{v}_{k_m}\tilde{w}_{k_n}^T\right), \tag{C.13}$$

where $\bar{v}_k = \mathbf{D}_k v_k$. With the same arguments used for the previous part $\lim_{N\to\infty} S_{m,n\ vD}(N) = 0$.

Continuing with $S_{m,n\ w}(N)$

$$S_{m,n\ w}(N) = \frac{1}{N}\sum_{k=0}^{N-1}\left(\tilde{w}_{k_m}z_{k_n}^T\tilde{\mathbf{C}}^T + \tilde{w}_{k_m}v_{k_n}^T\mathbf{D}_{k_n}^T + \tilde{w}_{k_m}\tilde{w}_{k_n}^T\right), \tag{C.14}$$

z_{k_n} and $\tilde{w}_{k_n}$ are square integrable variables such that $\sup_{k\geq 0}\mathbb{E}\left(\tilde{w}_k\tilde{w}_k^T\right) \leq C < \infty$, and $\lim_{N\to\infty}\frac{1}{N}\sum_{k_l}\|z_{k_l}\|^2 \leq C < \infty$. Also they are $\mathcal{Y}_k$-measurable and $\mathbb{E}\left(\tilde{w}_k|\mathcal{Y}_{k-1}\right) = 0$. So using Lemma 3 of [4] (as $k_m > k_n\ \forall k$)

$$\lim_{N\to\infty}\frac{1}{N}\sum_{k=0}^{N-1}\left(\tilde{w}_{k_m}z_{k_n}^T\tilde{\mathbf{C}}^T\right) = 0. \tag{C.15}$$

Also $\tilde{w}_{k_n}$ and v_k are Gaussian white noise, so they are independent and with zero mean, thus

$$\lim_{N\to\infty} S_{m,n\ w}(N) = 0. \tag{C.16}$$

Finally,

$$S_{m,n\ z}(N) = \tilde{\mathbf{C}}\tilde{\mathbf{A}}^{m+n-2}\frac{1}{N}\sum_{k=0}^{N-1}\left(z_{k_n}v_{k_n}^T\mathbf{D}_{k_n}^T + \tilde{\mathbf{A}}z_{k_n}\tilde{w}_{k_n}^T\right), \tag{C.17}$$

expressed as function of the step $k_n - 1$

$$S_{m,n\ z}(N) = \tilde{\mathbf{C}}\tilde{\mathbf{A}}^{m+n-1}\frac{1}{N}\sum_{k=0}^{N-1}\left(\left(\tilde{\mathbf{A}}z_{k_n-1} + \mathbf{B}_{k_n-1}v_{k_n-1}\right)v_{k_n}^T\mathbf{D}_{k_n}^T + \left(\tilde{\mathbf{A}}z_{k_n-1} + \mathbf{B}_{k_n-1}v_{k_n-1}\right)\tilde{w}_{k_n}^T\right). \tag{C.18}$$

Using $\tilde{v}_k$ and $\bar{v}_k$,

$$S_{m,n\ z}(N) = \tilde{\mathbf{C}}\tilde{\mathbf{A}}^{m+n-1}\frac{1}{N}\sum_{k=0}^{N-1}\left(\left(\tilde{\mathbf{A}}z_{k_n-1} + \tilde{v}_{k_n-1}\right)\bar{v}_{k_n}^T + \left(\tilde{\mathbf{A}}z_{k_n-1} + \tilde{v}_{k_n-1}\right)\tilde{w}_{k_n}^T\right). \tag{C.19}$$

$\tilde{\mathbf{A}}z_{k_n-1}+\tilde{v}_{k_n-1}$, $\tilde{v}_{k_n}$ and $\tilde{w}_{k_n}$ are square integrable variables such that $\sup_{k\geq 0}\mathbb{E}\left(\tilde{w}_k\tilde{w}_k^T\right) \leq C < \infty$, $\sup_{k\geq 0}\mathbb{E}\left(\tilde{v}_k\tilde{v}_k^T\right) \leq C < \infty$ and $\lim_{N\to\infty}\frac{1}{N}\sum_{k=0}^{N-1}\|\tilde{\mathbf{A}}z_k + \tilde{v}_k\|^2 \leq C < \infty$. Also they are $\mathcal{Y}_k$-measurable, with $\mathbb{E}\left(\tilde{w}_k|\mathcal{Y}_{k-1}\right) = 0$ and $\mathbb{E}\left(\tilde{v}_k|\mathcal{Y}_{k-1}\right) = 0$. Thus, using the Lemma 3 of [4]

$$\lim_{N\to\infty} S_{m,n\ z}(1) = 0. \tag{C.20}$$

All the parts converge to zero, consequently $S_{m,n} = o(1)$ converges to zero.

References

[1] G. Acar and B. F. Feeny. Floquet-based analysis of general responses of the mathieu equation. *Journal of Vibration and Acoustics*, 138(4), 2016.

[2] M. S. Allen, M. W. Sracic, S. Chauhan, and M. H. Hansen. Output-only modal analysis of linear time-periodic systems with application to wind turbine simulation data. *Mechanical Systems and Signal Processing*, 25(4):1174–1191, 2011.

[3] C. Bak, F. Zahle, R. Bitsche, T. Kim, A. Yde, L. C. Henriksen, M. H. Hansen, J. P. A. A. Blasques, M. Gaunaa, and A. Natarajan. The dtu 10-mw reference wind turbine. In *Danish wind power research 2013*, 2013.

[4] A. Benveniste and L. Mevel. Nonstationary consistency of subspace methods. *IEEE Transactions on Automatic Control*, 52(6):974–984, 2007.

[5] M. Bertelè and C. L. Bottasso. Automatic detection and correction of aerodynamic and inertial rotor imbalances in wind turbine rotors. In *Journal of Physics: Conference Series*, page 032100. IOP Publishing, 2022.

[6] G. Bir. Multi-blade coordinate transformation and its application to wind turbine analysis. In *46th AIAA Aerospace Sciences Meeting and Exhibit*, [Reston, VA], 2008. [American Institute of Aeronautics and Astronautics].

[7] S. Bittanti and P. Colaneri. Invariant representations of discrete-time periodic systems. *Automatica*, 36(12):1777–1793, 2000.

[8] R. Brincker and C. Ventura. *Introduction to operational modal analysis*. Wiley, Chichester West Sussex, 2015.

[9] E. Di Lorenzo. *Operational Modal Analysis for rotating machines*. PhD thesis, University of Naples" Federico II, 2017.

[10] M. Döhler and L. Mevel. Efficient multi-order uncertainty computation for stochastic subspace identification. *Mechanical Systems and Signal Processing*, 38(2):346–366, 2013.

[11] R. Ernst, P. Lauridsen, C. Klein, and B. Buffetti. The effect of damage position on operational modal analysis of wind turbine blades for shm. In *Journal of Physics: Conference Series*, page 032099. IOP Publishing, 2022.

[12] G. Floquet. Sur la théorie des équations différentielles linéaires. In *Annales Scientifiques de L'École Normale Supérieure*, volume 8, pages 3–132, 1879.

[13] S. Greś, M. Döhler, P. Andersen, and L. Mevel. Kalman filter-based subspace identification for operational modal analysis under unmeasured periodic excitation. *Mechanical Systems and Signal Processing*, 146:106996, 2021.

[14] S. Greś, M. Döhler, and L. Mevel. Uncertainty quantification of the modal assurance criterion in operational modal analysis. *Mechanical Systems and Signal Processing*, 152:107457, 2021.

[15] M. Hartvig Hansen and L. Christian Henriksen. Basic DTU wind energy controller. 2013.

[16] A. Jhinaoui, L. Mevel, and J. Morlier. A new ssi algorithm for lptv systems: Application to a hinged-bladed helicopter. *Mechanical Systems and Signal Processing*, 42(1-2):152–166, 2014.

[17] B. J. Jonkman. Turbsim user's guide. Technical report, National Renewable Energy Lab.(NREL), Golden, CO (United States), 2006.

[18] J. Kusnick, D. E. Adams, and D. T. Griffith. Wind turbine rotor imbalance detection using nacelle and blade measurements. *Wind Energy*, 18(2):267–276, 2015.

[19] N. Myrent, D. E. Adams, and D. T. Griffith. Wind turbine blade shear web disbond detection using rotor blade operational sensing and data analysis. *Philosophical Transactions of the Royal Society A: Mathematical, Physical and Engineering Sciences*, 373(2035):20140345, 2015.

[20] National Renewable Energy Laboratory - NREL. Openfast v2.5.0. `https://github.com/OpenFAST/openfast/releases/tag/v2.5.0`. Accessed: 2021-06-03.

[21] M. Ozbek and D. J. Rixen. Operational modal analysis of a 2.5 mw wind turbine using optical measurement techniques and strain gauges. *Wind Energy*, 16(3):367–381, 2013.

[22] M. Pastor, M. Binda, and T. Harčarik. Modal assurance criterion. *Procedia Engineering*, 48:543–548, 2012.

[23] B. Peeters and G. de Roeck. Reference-based stochastic subspace identification for output-only modal analysis. *Mechanical Systems and Signal Processing*, 13(6):855–878, 1999.

[24] E. Reynders, R. Pintelon, and G. de Roeck. Uncertainty bounds on modal parameters obtained from stochastic subspace identification. *Mechanical Systems and Signal Processing*, 22(4):948–969, 2008.

[25] R. Riva, S. Cacciola, and C. Bottasso. Periodic stability analysis of wind turbines operating in turbulent wind conditions. *Wind Energy Science*, 1:177–203, 2016.

[26] R. Riva, S. Cacciola, and A. Croce. High-resolution periodic mode shapes identification for wind turbines. In *Journal of Physics: Conference Series*, volume 1037, page 062002. IOP Publishing, 2018.

[27] U. Saetti and M. Lovera. Time-periodic and high-order time-invariant linearized models of rotorcraft: A survey. *Journal of the American Helicopter Society*, 67(1):1–19, 2022.

[28] P. F. Skjoldan and O. A. Bauchau. Determination of modal parameters in complex nonlinear systems. 2011.

[29] P. F. Skjoldan and M. H. Hansen. On the similarity of the Coleman and Lyapunov–Floquet transformations for modal analysis of bladed rotor structures. *Journal of Sound and Vibration*, 327(3):424–439, 2009.

[30] P. F. Skjoldan and M. H. Hansen. Implicit floquet analysis of wind turbines using tangent matrices of a non–linear aeroelastic code. *Wind Energy*, 15(2):275–287, 2012.

[31] S. Särkkä and A. Solin. *Applied stochastic differential equations*. Cambridge university press, 2019.

[32] D. Tcherniak. Rotor anisotropy as a blade damage indicator for wind turbine structural health monitoring systems. *Mechanical Systems and Signal Processing*, 74:183–198, 2016.

[33] D. Tcherniak, S. Chauhan, and M. H. Hansen. Applicability limits of operational modal analysis to operational wind turbines. In *Structural Dynamics and Renewable Energy, Volume 1*, pages 317–327. Springer, 2011.

[34] D. Tcherniak and G. C. Larsen, editors. *Application of OMA to an Operating Wind Turbine: now including Vibration Data from the Blades*, 2013.

[35] D. Tcherniak, S. Yang, and M. Allen. Experimental characterization of operating bladed rotor using harmonic power spectra and stochastic subspace identification. In *Proc. International Conference on Noise and Vibration Engineering (ISMA)*, 2014.

[36] Technical University of Denmark - DTU. dtu-10mw-rwt. `https://rwt.windenergy.dtu.dk/dtu10mw/`

`dtu-10mw-rwt`. Accessed: 2021-06-03.

[37] G. J. van der Veen, J.-W. van Wingerden, and M. Verhaegen, editors. *Closed-loop system identification of wind turbines in the presence of periodic effects*, 2010.

[38] P. van Overschee and B. de Moor. Subspace algorithms for the stochastic identification problem. *Automatica*, 29(3):649–660, 1993.

[39] N. M. Wereley and S. R. Hall. Linear time periodic systems: transfer function, poles, transmission zeroes and directional properties. In *American Control Conference*, pages 1179–1184. IEEE, 1991.

[40] S. Yang, D. Tcherniak, and M. S. Allen. Modal analysis of rotating wind turbine using multiblade coordinate transformation and harmonic power spectrum. In *Topics in Modal Analysis I, Volume 7*, pages 77–92. Springer, 2014.